SN 2024iss: A Double-peaked Type IIb Supernova with Evidence of **Circumstellar Interaction**

Liyang Chen^{1*}, Xiaofeng Wang^{1**}, Qinyu Wu^{2,3}, Moira Andrews^{4,5}, Joseph Farah^{4,5}, Paolo Ochner^{6,7}, Andrea Reguitti^{8,7}, Thomas G. Brink⁹, Jujia Zhang^{10,11,12}, Cuiying Song¹, Jialian Liu¹, Alexei V. Filippenko⁹, David J. Sand^{1,3}, Irene Albanese⁶, Kate D. Alexander^{1,3}, Jennifer Andrews^{1,4}, K. Azalee Bostroem^{13,15}, Yongzhi Cai (療水 芸)^{10,11,12}, Collin Christyl³, Ali Esamdin ^{16,3}, Andrea Farinal⁷, Noah Franz^{1,3}, D. Andrew Howell^{4,5}, Brian Hsul³, Maokai Hu¹, Abdusamatjan Iskandar^{16,3}, Liping Li^{10,11,12}, Gaici Li¹, Dongyue Li², Wenxiong Li², Jinzhong Liu^{16,3}, Curtis McCully⁴, Megan Newsome^{1,8}, Yuan Qi Ni¹⁹, Andrea Pastorello⁷, Estefania Padilla Gonzalez²⁰, Jeniveve Pearson^{1,3}, Haowei Peng¹, Conor Ransome^{1,3}, Manisha Shrestha^{21,22}, Nathan Smith^{1,3} Bhagya Subrayan^{1,3}, Giacomo Terrerar^{2,3}, Giorgio Valerin⁷, J. Vink^{2,4,25,26,18}, Sergiy S. Vasylyev⁹, Letian Wang¹⁶, Zhenyu Wang^{10,3}, Hao Wang^{2,7}, J. Craig Wheeler¹⁸, Kathryn Wynn^{4,5}, Danfeng Xiang^{1,28}, Shengyu Yan¹, Weimin Yuan^{2,3}, Juan Zhang^{2,7}, WeiKang Zheng⁹, and Yu Zhang^{16,3} (Affiliations can be found after the references)

October 27, 2025

ABSTRACT

Alims. We present optical, ultraviolet, and X-ray observations of supernova (SN) 2024iss, a Type IIb SN that shows a prominent double-peaked be envelope radius and mass-loss rate with those of other Type IIb SNe to explore the relationships between the progenitor envelope and the circumstellar material (CSM).

Hesults. The shock-cooling peak in the V-band light curve reached M_V = -17.33 ± 0.26 mag, while the ⁵⁶Ni-powered second peak attained M_V = -17.43 ± 0.26 mag. Early spectra show an photospheric velocity of ~ 19, 400 km s⁻¹ at 3.82 days from the Ho P Cygni profile. The Balmer Inserpensia at least +87 days after the explosion, characterizing hydrogen-rich ejecta. Modeling the first light-curve peak with the shock-cooling model suggests an extended hydrogen envelope with a mass of 0.11 ± 0.013 M₀ and a relatively low ejecta mass of 1.272 ± 0.343 M₀. X-ray observations reveal bright thermal bremstrahlung emission and indicates a mass-loss at of 1.6 x 10⁻⁷ M₀ y⁻⁷ withing the second light-curve peak with a free-free wold. We words. Sand¹³, Irene Albanese⁶, Kate D. Alexander¹³, Jennifer Andrews¹⁴, K. Azalee Bostroem^{13, 15}, Yongzhi Cai (蔡永 志)^{10,11,12}, Collin Christy¹³, Ali Esamdin^{16,3}, Andrea Farina¹⁷, Noah Franz¹³, D. Andrew Howell^{4,5}, Brian Hsu¹³,

transitional subclass whose spectrophotometic properties lie between those of the Type II and Ib SNe (Filippenko 1997; Gal-Yam 2017). The spectra of Type IIb SNe initially exhibit strong hydrogen features, with no evidence of helium. The hydrogen lines persist only for the first few weeks, which is much shorter compared to that observed in Type II/IIP SNe. P Cygni features of He I appear in the spectra at about two weeks after explosion, while hydrogen lines become significantly weakening at the same time (see, e.g., Filippenko 1997).

SNe has been partially stripped, thus providing an important approach to test the mechanisms that can dramatically strip the outer envelopes of massive progenitor stars. The remarkable transformation between the hydrogen- and helium-dominated spectroscopic phases was initially revealed by the extensive observing campaign on SN 1993J (Filippenko et al. 1993, 1994; Woosley et al. 1994; Barbon et al. 1995; Richmond et al. 1996; Matheson et al. 2000). Thanks to the transient-alert stream produced by high-cadence wide field sky surveys such as the Palomar Transient Factory (PTF, Rau et al. 2009; Law et al. 2009) and later the Zwicky Transient Facilities (ZTF, Bellm et al.

E-mail: chenly23@mails.tsinghua.edu.cn

^{**} E-mail: wang xf@mail.tsinghua.edu.cn

2019; Graham et al. 2019), large samples of SNe IIb have been studied, including SNe 2011dh (Arcavi et al. 2011; Ergon et al. 2014), 2011fu (Kumar et al. 2013; Morales-Garoffolo et al. 2015), 2013df (Morales-Garoffolo et al. 2014; Szalai et al. 2016), 2016gkg (Tartaglia et al. 2017; Bersten et al. 2018; Sravan et al. 2018), 2020acat (Medler et al. 2022) and 2024uwq (Subrayan et al. 2025). Detailed analyses of the homogeneity and diversity of SNe IIb have also been preformed based on a larger sample (e.g., Shivvers et al. 2019).

One way to investigate the nature of Type IIb SNe can be facilitated by analyzing the archival pre-explosion images. By fitting stellar evolutionary tracks to the spectral energy distribution (SED) extracted at the exact location of the SN on the archival images taken by the *Hubble Space Telescope* (*HST*), various studies suggest that the progenitor star of SNe IIb tend to be yellow (or even cooler) supergiants, for example, SNe 1993J (Maund et al. 2004), 2013df (Van Dyk et al. 2014), 2016gkg (Kilpatrick et al. 2017; Tartaglia et al. 2017), 2017gkk (Niu et al. 2024) and 2024abfo (Reguitti et al. 2025; Niu et al. 2025).

A more general approach to investigate the nature of the progenitor can be achieved by fitting the early-time emissions of the SN explosion with a shock-cooling model. This process characterizes the energy emitted by the shock breakout deposited in the ejecta and describes how such energy diffuses out as the ejecta expands and cools (see, e.g., Waxman & Katz 2017 for a review). The early luminosity evolution of SNe IIb often manifests itself as a double-peaked light curve, where the first peak is powered by the cooling of the extended envelope of the progenitor star heated by the shock, namely the shock-cooling emission (SCE, Soderberg et al. 2012). Various semi-analytic models have been developed within the framework of shock cooling and were used to fit the early light curves of core-collapse (CC) SNe.

Piro et al. (2021) introduced a two-zone model with a broken power law to characterize the radial density structure of the envelope. This model builds on the earlier works of Piro (2015) and Nakar & Piro (2014). Meanwhile, Sapir & Waxman (2017) extended the earlier work of Rabinak & Waxman (2011) to a longer regime of validity, introducing two choices of the polytropic index: n = 3 for radiative envelopes (e.g., BSGs) and n = 3/2 for convective envelopes (e.g., RSGs). Morag et al. (2023) further developed the framework established in Sapir & Waxman (2017) by considering the effects of strong blanketing of numerous iron absorption lines in the near ultraviolet (UV) to optical wavelength ranges and the multizone dynamics, increasing the feasibility of the model at early phases. Farah et al. (2025b) developed a framework for shock-cooling fitting of SNe IIb, employing various models to constrain the envelope mass and radius. Moreover, Nagy & Vinkó (2016) developed a semi-analytical model to constrain the nature of the envelope, by considering a dense inner region and an extended low-mass envelope.

These models of the early luminosity evolution of SNe IIb generally suggest that the extended hydrogen envelope associated with their first light curve peak have masses of 10^{-2} - $10^{-1}M_{\odot}$ and radii of $100-500\,R_{\odot}$, which are both broadly consistent with the results of pre-explosion imaging, although some discrepancies remain unresolved. Alternative interpretations of the early

light curve peak have also been proposed, including a bimodal radial distribution of ⁵⁶Ni (Orellana & Bersten 2022) and thermal energy deposited by the shock as it propagates through the envelope (Liu et al. 2025).

Owing to pre-explosion mass loss and partial envelope stripping, some SNe IIb also exhibit signatures of circumstellar material (CSM), offering valuable insights into pre-explosion massloss history of their progenitor systems (Smith 2017).

X-ray emission provides another important trace of the ejecta-CSM interaction. Fransson et al. (1996) analyzed the X-ray emission of SN 1993J and attributed it to the thermal bremsstrahlung produced by the forward shock. This framework was extended in studies of SNe 2011dh (Soderberg et al. 2012) and 2013df (Kamble et al. 2016), further supporting the role of X-ray observations in providing critical constraints on the electron number density of the CSM around Type IIb SNe. Dwarkadas (2025) compiled the early X-ray light curves of interacting CCSNe and found no compelling evidence for non-thermal X-ray emission in SNe IIb.

The mechanism stripping the envelopes of the progenitor star remains uncertain. The removal of the progenitor's envelope and the formation of circumstellar material (CSM) generally result from two categories: single-star or binary interaction driven mechanisms. In the framework of wind-driven mass loss (e.g., Woosley et al. 1993; Georgy 2012; Yoon 2017), the stripping of a star can be rather intense and may indicate a massive progenitor such as a Wolf-Rayet star, as seen in events like the first hypernova (Hamuy et al. 2009). Additionally, eruptive mass loss just prior to the terminal explosion may be triggered by processes including pulsation-driven superwinds (Yoon & Cantiello 2010) or core neutrino emission (Moriya 2014).

Alternatively, binary interaction has gained increasing support in recent years as a more prevalent explanation for envelope stripping (Podsiadlowski 1992; Smith 2014; Sravan et al. 2020; Dessart et al. 2024). Sana et al. (2012) indicates that more than 70% massive stars undergo mass exchange with a companion, with about one-third resulting in binary mergers. Direct imaging has confirmed companion stars in some Type IIb progenitors, such as those of SN 1993J (Maund & Smartt 2009) and SN 2001ig (Ryder et al. 2018). Moreover, binary scenarios naturally explain the observed correlations between CSM properties and the residual envelope of the progenitor.

Chevalier & Soderberg (2010) were the first to classify SNe IIb into two subtypes based on the prominence of their shock-cooling emission, and investigated their associated X-ray properties. The extended subtype (Type eIIb) exhibits a pronounced shock-cooling peak in the early light curve, indicating a relatively massive hydrogen envelope ($\geq 0.1 M_{\odot}$) and a large progenitor radius ($\sim 100-1000\,R_{\odot}$). These events typically show thermal X-ray emission. In contrast, objects belonging to the compact subtype (Type cIIb) display a weaker or no signature of shock cooling, indicating smaller sizes of their progenitors.

Following this classification, Soderberg et al. (2012) and Kamble et al. (2016) found that Type eIIb SNe generally exhibit stronger X-ray emission and are surrounded by denser CSM. The distinction between Type eIIb and Type cIIb is further supported by Maeda et al. (2015) and Ouchi & Maeda (2017), which show that the initial orbital separation affects the residual envelope

mass and pre-explosion mass loss. In this framework, closer binaries tend to produce more stripped, compact progenitors with lower mass-loss rates. A parallel study by Yoon et al. (2017) proposed that Type eIIb SNe originate from systems undergoing late Case B mass transfer and evolve into red supergiants (RSGs), while Type cIIb events would result from early Case B transfer and evolve into blue or yellow supergiants (BSGs or YSGs). Nevertheless, the sample size of SNe IIb is still limited, and events with comprehensive optical and X-ray observations are even sparse. Further studies of the relationship between the envelope and the CSM will require a larger, well-characterized sample.

In this article, we present and analyze the spectrophotometric and X-ray observations of SN 2024iss, a nearby type IIb SN with a prominent double peak in optical bands, and it exhibits bright thermal X-ray emission comparable with SN 1993J. Basic information about SN 2024iss is provided in Section 2.1. The details of the observations and data reduction are described in Section 2. In Section 3, we analyze the multiband light curves and the evolution of the bolometric luminosity. The spectral evolution and comparisons with other well-observed SNe IIb are discussed in Section 4. In Section 5, we model the early shock-cooling emission peak. The X-ray properties are inferred in Section 6. In Section 7, we discuss possible mass-loss mechanisms for SN 2024iss. Finally, the main conclusions are summarized in Section 8.

2. Observations and Data Reduction

2.1. Discovery and Host Galaxy

SN 2024iss was discovered on UT 2024 May 12 21:37 (MJD 60442.901) by the Gravitational-wave Optical Transient Observer (GOTO; Steeghs et al. 2022). Approximately six hours before the reported discovery, the SN emission was recorded by a public outreach telescope located at the Xinglong Observatory, as detailed in Section 2. The SN exploded at celestial coordinates $\alpha=12^{\rm h}59^{\rm m}06''.130$, $\delta=+28^{\circ}48'42''.62$, in the outskirts of the nearby dwarf galaxy WISEA J125906.48+284842.6 (redshift z=0.003334).

Assuming a flat Λ cold dark matter (Λ CDM) model with $H_0 = 73.0 \text{ km s}^{-1} \text{Mpc}^{-1}$, $\Omega_{\text{m}} = 0.27$, and $\Omega_{\Lambda} = 0.73$ (Spergel et al. 2007), we adopt a distance of 13.4 \pm 1.6 Mpc, based on the Local Group velocity (Fixsen et al. 1996), as inquired from the NASA/IPAC Extragalactic Database (NED).

Considering the low redshift of SN 2024iss, we adopt an additional 10% uncertainty in distance to account for the effect of the peculiar velocity. We add this systematic uncertainty and the error in the Local Group distance in quadrature to obtain the final uncertainty in the distance to SN 2024iss. This yields a distance modulus of 30.64 ± 0.26 mag, which is used throughout this paper.

The Galactic reddening toward the line sight of SN 2024iss was estimated as $E(B-V)=0.0084\,\mathrm{mag}$ based on the extinction map derived by Schlafly & Finkbeiner (2011). We neglect the reddening of the host galaxy, as no strong Na I D absorption features can be identified at the redshift of the host (see Section 4). Adopting the $R_V=3.1$ extinction law (Cardelli et al. 1989), this results in an extinction of $A_V=0.026\,\mathrm{mag}$.

Table 1: Basic properties of SN 2024iss

Host galaxy	WISEA J125906.48+284842.6
RA (J2000)	$12^h 59^m 06.^s 130$
DEC (J2000)	+28°48′42.′′62
Distance	$13.4 \pm 1.6 \mathrm{Mpc}$
Distance modulus	$30.64 \pm 0.26 \text{ mag}$
Redshift	0.003334
$E(B-V)_{MW}$	$0.0084 \pm 0.0002 \text{ mag}$
$E(B-V)_{host}$	0.0
Explosion time	MJD $60442.21 \pm 0.44 \ (2024/05/12)$
V_{max}	MJD 60460.63 (2024/05/30)

The last non-detection was reported by the All-Sky Automated Survey for Supernovae (ASAS-SN; Kochanek et al. 2017) with a g-band limiting magnitude of 18.24 mag, on 2024 May 11 18:29 (MJD 60441.770), \sim 0.87 days before the first detection in Xinglong (MJD = 60442.645). Throughout this paper, all phases are given relative to the estimated explosion time of SN 2024iss, defined as the midpoint between the last non-detection and the first detection, i.e., MJD 60442.208 \pm 0.438. A more detailed estimation of t_0 by fitting a shock-cooling model to the early light curves of SN 2024iss will be presented in Section 5. Basic observational properties of SN 2024iss are summarized in Table 1.

2.2. Optical Photometry

The observing campaign on SN 2024iss started at approximately six hours before the reported discovery. Follow-up photometry was obtained by the 0.8 m Tsinghua University-NAOC telescope (TNT; Huang et al. 2012) at Xinglong Station, the Lijiang 2.4 m telescope (LJT; Fan et al. 2015) of Yunnan Astronomical Observatories, the Nanshan One-meter Wide-field Telescope (NOWT; Bai et al. 2020), the 0.36 m reflector of the Tsinghua University (SNOVA) at Nanshan Station of Xinjiang Astronomical Observatory, the Schmidt 67/91 cm Telescope (67/91-ST), the Copernico 1.82 m telescope at the Asiago Astrophysical Observatory, and the 3.58 m Telescopio Nazionale Galileo (TNG; Barbieri et al. 1994) on the island of La Palma and the Las Cumbres Observatory's global network of robotic telescopes (LCO; Brown et al. 2013) through the Global Supernova Project.

Optical images were pre-processed with standard procedures, which include bias subtraction, flat-field correction and cosmic-ray removal. We used a custom ZURTYPHOT pipeline (Mo et al. in prep.) to reduce the TNT images. The AUTOmated Photometry Of Transients (AutoPhOT) pipeline (Brennan & Fraser 2022) was implemented to extract the photometry from the images obtained by the XL_106, LJT, 67/91-ST, Copernico and TNG. As XL_106 is equipped with *RGB* filters, we calibrate the *R*-, *G*-, and *B*-band photometry to the *r*-, *V*-, and *g*-band under the Sloan Digital Sky Survey (SDSS) photometric system (Fukugita et al. 1996) in AB magnitudes (Oke & Gunn 1983), respectively, following the prescriptions in Li et al. (2024). Considering SN 2024iss exploded in the outskirts of a faint dwarf galaxy, template subtraction

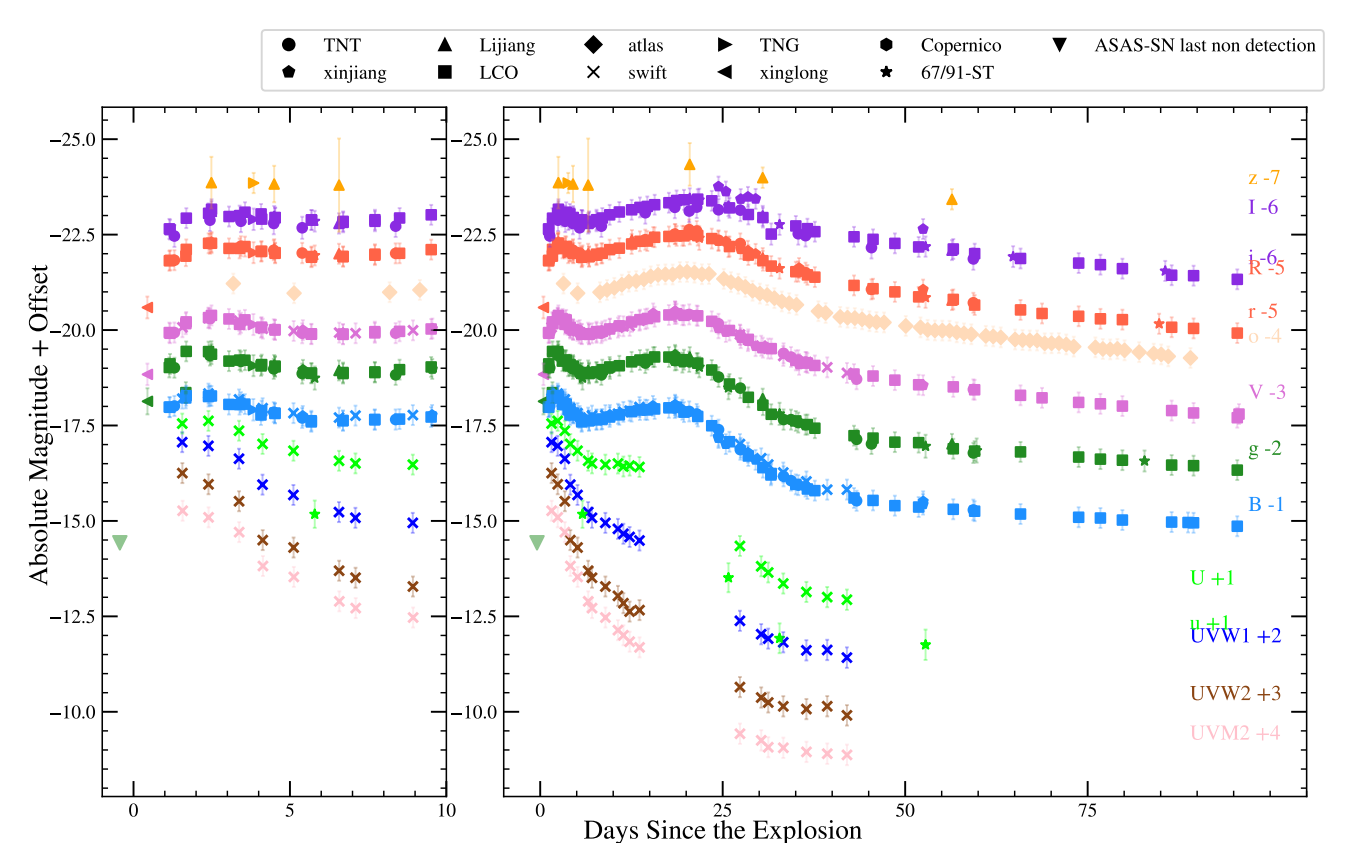


Fig. 1: Optical light curves of SN 2024iss. Left panel: the early-time multiband photometry within the first ten days. Right panel: the multiband light curves of SN 2024iss within the first \sim 100 days. All magnitudes were corrected for the Galactic extinction. For better display, light curves in different bandpasses were shifted vertically by arbitrary numbers as labeled on the right. Facilities used to obtain the photometry are indicated by the legend. The last non-detection from ASAS-SN is marked by the green inverted triangle.

is not necessary. The instrumental magnitudes of SN 2024iss were calibrated using the AAVSO Photometric All Sky Survey (APASS) DR9 Catalogue (Henden et al. 2016). The final BV- and gri- band magnitudes of SN 2024iss were calibrated against local bright comparison stars, and were transformed to the standard Johnson (Vega magnitude; Johnson et al. 1966) and SDSS (AB magnitude; Fukugita et al. 1996) systems, respectively. We also include the near-infrared (NIR) band photometry from Yamanaka et al. (2025) for bolometric luminosity calculation in Section 3.3.

SN 2024iss was also observed with the UVOT (Roming et al. 2005) board on the Neil Gehrels Swift Observatory (Swift; Gehrels et al. 2004), using a 5" aperture to measure magnitudes in *uvw*1, *uvw*2, *uvm*2, *u*, *b*, and *v* band-passes. Photometric data were extracted with HEASOFT¹ and the latest Swift calibration database² (Breeveld et al. 2011). In addition, high-cadence *o*-band photometry from ATLAS (Tonry et al. 2018) was included in our dataset. We list the photometry of SN 2024iss in Table 2. Figure 1 shows the multiband light curves of SN 2024iss.

Table 2: Photometric Observations of SN 2024iss

	L				
MJD^a	Phase ^b	Filter	Mag.	Mag. error	Instrument
60442.65	0.44	r	15.07	0.12	XL_106
60442.65	0.44	V	14.83	0.11	XL_106
60442.65	0.44	g	14.54	0.22	XL_106
60443.35	1.14	В	13.69	0.02	LCO
60443.35	1.14	V	13.73	0.02	LCO
60443.35	1.14	g	13.65	0.01	LCO
60443.35	1.14	r	13.84	0.01	LCO
60443.35	1.14	i	14.0	0.02	LCO
	•••	•••		•••	

Notes. ^(a) This table is available in its entirety in machine-readable form. ^(b) Time respect to MJD=60,442.21.

2.3. Optical Spectroscopy

Our spectral sequence of SN 2024iss consists of 51 spectra, spanning the phase from $t \approx 1$ days to 87 days after the explosion. The data set is obtained by various facilities including the Beijing Faint Object Spectrograph and Camera (BFOSC) on the Xinglong 2.16 m telescope (XLT;) the Kast double spectrograph (Miller & Stone 1994) mounted on the Shane 3 m telescope

¹ https://www.swift.ac.uk/analysis/software.php

² https://heasarc.gsfc.nasa.gov/docs/heasarc/caldb/swift/

at Lick Observatory, the Yunnan Faint Object Spectrograph and Camera (YFOSC) on the Lijiang 2.4 m telescope (LJT; Wang et al. 2019), the FLOYDS spectrographs (Brown et al. 2013) on the 2 m Faulkes Telescopes South and North (FTS and FTN), the Gemini Multi-Object Spectrograph (GMOS; Hook et al. 2004) on the Gemini North Telescope (GNT), the B&C spectrograph on the 1.22 m Galileo Telescope (GT), the DOLORES (Device Optimised for the LOw RESolution) on the 3.5 m Telescopio Nazionale Galileo (TNG), the Low Resolution Spectrograph 2 (LRS2; Chonis et al. 2014) mounted on the Hobby-Eberly Telescope (HET; Ramsey et al. 1998) located at McDonald Observatory, Binospec (Fabricant et al. 2019) at the MMT Observatory, the Boller and Chivens Spectrograph (B&C) on the University of Arizona's Bok 2.3 m telescope located at Kitt Peak Observatory, and the Multi-Object Double Spectrographs (MODS; Pogge et al. 2010) on the Large Binocular Telescope (LBT) located on Mt. Graham, Arizona USA. The observation log of optical spectroscopy is presented in Table A.3.

All spectra were processed following routines within IRAF (Tody 1986, 1993), custom Python and IDL codes³, including bias subtraction, flat-field correction, and cosmic-ray removal. The FLOYDS pipeline (Valenti et al. 2014) were used to reduce the FLOYDS spectra. Spectra taken with GNT + GMOS are reduced with the Data Reduction for Astronomy from Gemini Observatory North and South (DRAGONS; Labrie et al. 2019) package. The HET spectra was reduced by the Panacea pipeline⁴. Spectra taken with the Binospec on MMT are reduced using the Python-based package Pypeit (v1.17.4; Prochaska et al. 2020), while those taken with the MODS are bias and flat-field corrected using the modsCCDred package (Pogge 2019), then they are extracted and flux-calibrated with the standard IRAF routines. Wavelengths were calibrated using Fe/Ar or Fe/Ne lamp spectra taken on the same night. Flux calibration was achieved using standard stars observed at similar airmasses. We also remove the telluric features by scaling a mean telluric spectrum constructed from multiple observations of telluric standard stars to match the SN spectrum.

2.4. X-ray Observations

Immediately after the explosion of SN 2024iss, rapid followup observations in soft X-ray band were carried out by the Follow-up X-ray Telescope (FXT; Chen et al. 2020) on the Einstein Probe (EP) satellite (Yuan et al. 2022), the X-ray Telescope (XRT; Burrows et al. 2005) on the Swift satellite (Gehrels et al. 2004), and the Nuclear Spectroscopic Telescope Array (NuS-TAR; Harrison et al. 2013). Note that a prominent signal was detected by EP-FXT during its first epoch observations (corresponding to $t \approx +3$ days after the explosion). Integration of SN 2024iss by Swift-XRT was started approximately two days after the explosion. A total of 18 observations were conducted spanning the phases from days +2 to +34. We detected prominent signals in the first two time intervals, spanning from days +1.5 to +3.7 and +4.1 to +7.1, respectively. Rebinning the Swift XRT integration to the third time interval centered at day +11 reveals a rapid decline of the X-ray luminosity. We do not detect

any significant signal during the fourth time interval centered at day +35 after the explosion. Subsequent Swift observations conducted at $t \approx 207$ and 277 days did not detect any signals at the location of SN 2024iss. A log of the X-ray observations is provided in Table A.1.

The FXT data were reduced with the FXT data-analysis software (fxtsoftware v1.10)⁵ to produce high-level science products. Swift/XRT data were processed with the online XRT product builder⁶ (Evans, P. A. et al. 2007; Evans et al. 2009). NuS-TAR observations were analyzed with the standard NuSTAR data-analysis software (NuSTARDAS v2.1.2) to extract science products. We fit the energy spectrum with the tbabs*apec model⁷. The tbabs model computes the total cross section of the gas particles along the source-Earth line of sight that induce the X-ray absorption, including the Galactic, the host, and the matter surrounding the emitting source. The apec model calculation returns the emission spectrum produced by the collisionallyionized diffuse gas. The best-fit model parameters of X-ray spectrum are tabulated in Table A.2. Due to the limited photon counts and the restricted energy coverage of FXT (0.5-10 keV), the plasma temperature (kT) of SN 2024iss at each epoch cannot be reliably constrained independently. We therefore adopt a fixed plasma temperature to the temperature estimated from the second NuSTAR observation for all other observations. The neutral hydrogen column density from the Milky Way towards the direction of SN 2024iss is 7.5×10^{19} cm⁻² (Foight et al. 2016), as derived assuming it is linearly correlated with the Galactic reddening component, namely E(B-V) = 0.0084 mag.

3. Optical Photometry

3.1. Photometric Evolution

Figure 1 shows the UV and optical light curves of SN 2024iss. We divide the temporal evolution of the photometry into two phases, namely the early shock-cooling (from days 0 to 10 after the SN explosion) and the later radioactive decay phases. SN 2024iss was discovered very shortly after the explosion, following the serendipitous gVr-band images obtained on day 0.44, we continued the high-cadence multicolor photometric followup campaign on SN 2024iss and obtained the second epoch of observation on day 1.3. SN 2024iss reached the first V-band peak of -17.33 ± 0.26 mag on about day 2.4. This evolution is consistent with the cooling of a hot blackbody, where the peak of the emission shifts progressively to longer wavelengths as the temperature decreases.

At $t \approx 5$ days after the explosion, as photons escape from the expanding shock heated envelope, the SN luminosity becomes progressively dominated by the radioactive decay of ⁵⁶Ni, which powered the second peak of SN 2024iss. After correcting for extinction, the peak of the *V*-band light curve ($M_V = -17.43 \pm 0.26$) was reached on day 18.7. At $t \approx 50$ days after the explosion, the light curves of SN 2024iss in all observed bandpasses enter a linear decline phase, with a characteristic *V*-band decline rate of ~ 2.0 mag 100^{-1} day. As seen in other SNe IIb, SN 2024iss de-

https://github.com/ishivvers/TheKastShiv

⁴ https://github.com/grzeimann/Panacea

⁵ http://epfxt.ihep.ac.cn/analysis

⁶ https://www.swift.ac.uk/user_objects

⁷ https://heasarc.gsfc.nasa.gov/docs/xanadu/xspec/index.html

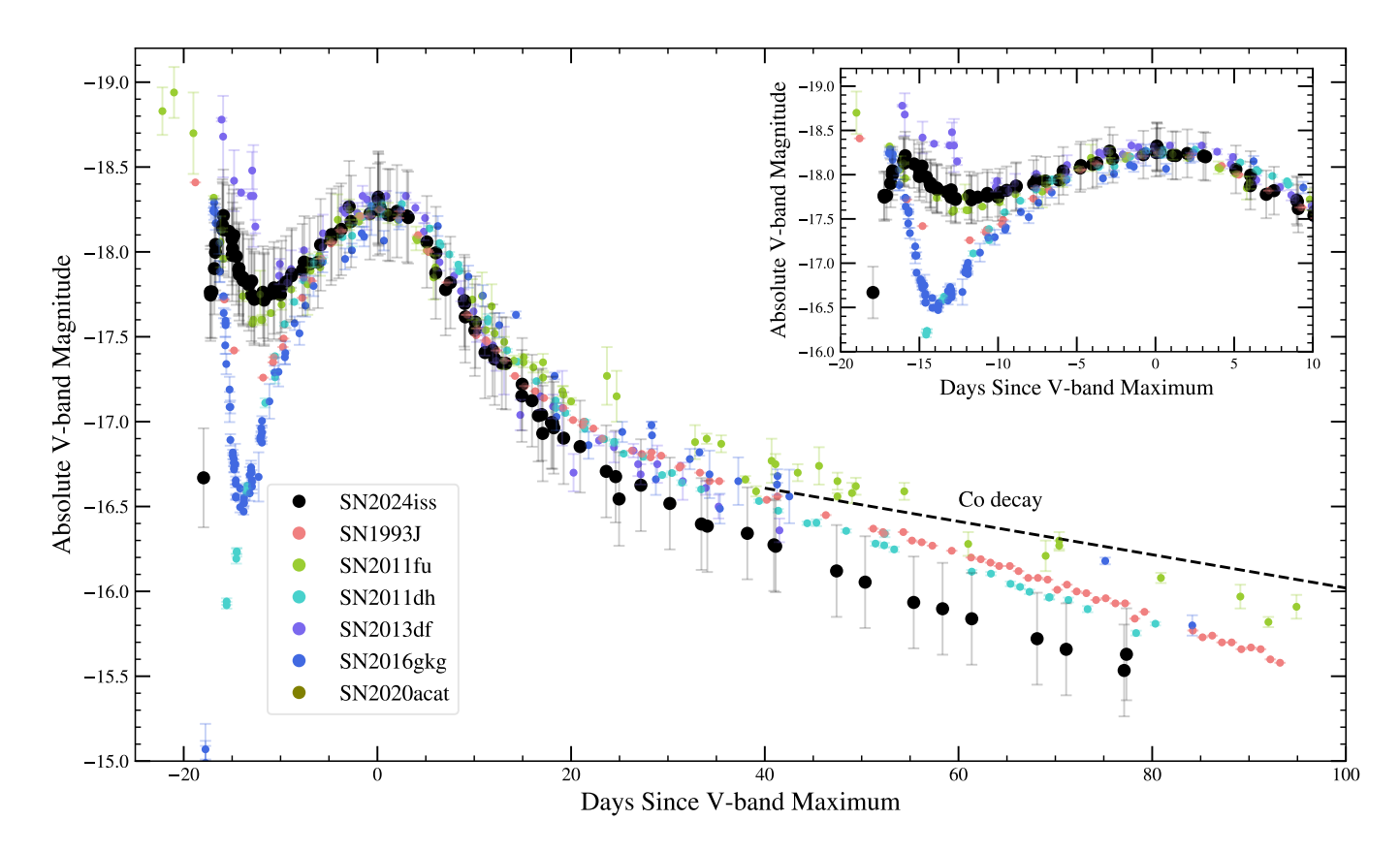


Fig. 2: The V-band light curve of SN 2024iss compared to those of well-sampled cases, i.e., the Type IIb SNe 1993J, 2011dh, 2013df, 2016gkg and 2020acat. The light curves of the comparison SNe have been shifted in both magnitude and time to align with the peak magnitude and the time of the V-band light curve peak of SN 2024iss. The black dashed line represents the expected decline rate of 56 Co (0.98 mag/100 day, Woosley et al. 1989). The upper-right inset shows a zoom-in of the first 30 days.

clines faster than the radioactive decay rate of $^{56}\text{Co} \rightarrow ^{56}\text{Fe}, 0.98$ mag/100 days.

Figure 2 compares the absolute *V*-band light curve of SN 2024iss with a sample of well-observed SNe IIb, including SNe 1993J (Richmond et al. 1996), 2011fu (Morales-Garoffolo et al. 2015), 2011dh (Ergon et al. 2014), 2013df (Morales-Garoffolo et al. 2014), 2016gkg (Arcavi et al. 2017; Bersten et al. 2018) and 2020acat (Medler et al. 2022). Basic observational properties of this SN sample are provided in Table 3. Considering the relatively large uncertainties in the estimation of the distance modulus among various cases, we arbitrarily shifted the light curve to match the peak of the *V*-band magnitude of SN 2024iss, and aimed to compare the morphology of the light curves of different SNe IIb.

SN 2024iss shows a prominent first peak, which is similar to that of SNe 1993J, 2011fu, 2013df and 2016gkg, but distinct from that of SNe 2011dh and 2020acat. According to Chevalier & Soderberg (2010), SNe IIb can be further classified into two subtypes, namely the extended-envelope (eIIb) and compact-envelope (cIIb) events. The prominent early peak of SN 2024iss indicates its extended-envelope nature. Among all the known cases that belong to the eIIb group, SN 2024iss is notable for its well-sampled first peak, with multiband photometry covering both the rise and the decline during the shock-cooling phase. The decline rate of the first peak in SN 2024iss is comparable to that of SN 2011fu. However, the former ex-

hibits a shorter decline time and a shallower subsequent valley compared to those observed in SNe 1993J and 2011fu. At the ⁵⁶Ni-powered phase, as illustrated in Figure 2, the *V*-band light curve of SN 2024iss displays remarkable similarities to those of other comparison SNe IIb. At the linear decline phase of the light curve (from ~60 days post-explosion), SN 2024iss exhibits a faster decline compared to that of other comparison SNe. A more detailed modeling of the initial and the secondary peaks, and the radioactive decay tail of the light curve of SN 2024iss, will be presented in Sections 5, 3.4, and 7.3, respectively.

3.2. Color Evolution

Figure 3 compares the extinction-corrected U-B, B-V, and g-r color curves of SN 2024iss with those of SNe 1993J, 2011fu, 2011dh, 2013df and 2016gkg. For better comparison, the V-R colors of SNe 1993J, 2011fu, 2013df and 2016gkg were converted to g-r using the transformation relations provided by Jordi et al. (2006).

As shown in the top panel of Figure 3, the U-B color of SN 2024iss displays a continuous increase until setting to a plateau at a maximum of $\sim 1.2 \pm 0.37$ mag at $t \approx 35$ days. The B-V and g-r colors of SN 2024iss show a similar evolution, with two distinct phases of increase of the color indices, which coincide with the first and second optical light curve peaks, respectively. In particular, the B-V and the g-r colors of

Time of the Second Peak $E(B-V)_{MW}$ $E(B-V)_{Host}$ SN **Explosion Time** Redshift m - MSource^a (MJD) (MJD) (mag) (mag) (mag) 1993J 49074.0 49095.0 -0.001130 27.31 0.0690 0.110 1,2,3 2011dh 55712.0 55732.0 0.001638 29.46 0.0310 0.040 4 2011fu 55825.0 55846.9 0.001845 34.36 0.0680 0.150 5,6 7,8 2013df 0.00239031.10 56450.0 56469.0 0.0170 0.081

Table 3: Properties of some typical Type IIb SNe Compared with SN 2024iss

Notes. (a) (1) Richmond et al. (1994); (2) Barbon et al. (1995); (3) Richmond et al. (1996); (4) Ergon et al. (2014); (5) Kumar et al. (2013); (6) Morales-Garoffolo et al. (2015); (7) Van Dyk et al. (2014); (8) Morales-Garoffolo et al. (2014); (9) Sravan et al. (2018); (10) Medler et al. (2022).

0.004900

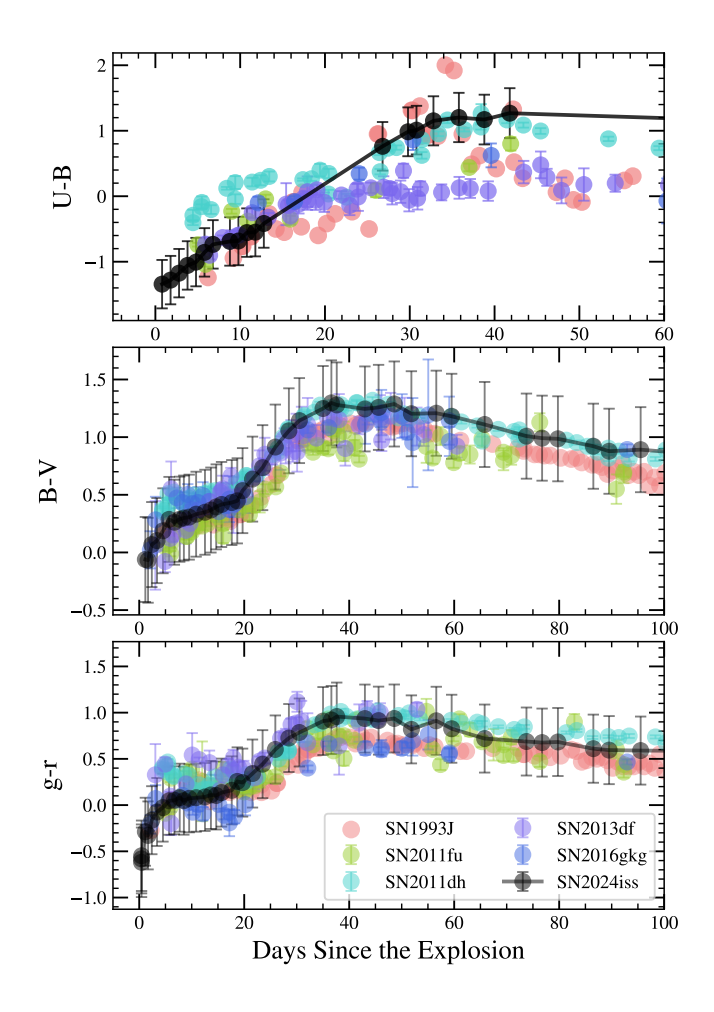
0.007932

57669.0

59208.7

32.11

32.74



2016gkg

2020acat

57651.2

59192.0

Fig. 3: Galactic reddening-corrected U-B, B-V, and g-r color curves of SN 2024iss, compared with Galactic reddening-corrected color curves of SNe 1993J, 2011fu, 2011dh, 2013df, and 2016gkg. For the purpose of display, the V-R color curve of SNe 1993J, 2011fu, 2013df and 2016gkg were converted to g-r using the transformation from Jordi et al. (2006).

SN 2024iss increase by ~ 0.35 mag and 0.67 mag within the first five days, respectively. Such an initial rise indicates a rapid decrease in photospheric temperature as fitted by a blackbody function (see Section 3.3 and Figure 4). From $t \approx 5$ to 20 days, both the B-V and g-r colors of SN 2024iss continue to become

redder, but at a much slower rate. Such a two-phase redward evolution in the early color curves is broadly consistent with the average behavior of the comparison SNe IIb shown in Figure 3. In contrast, a blueward color evolution between the two rapid increases in B-V and g-r is reported in SNe 2022crv (Dong et al. 2024) and 2024uwq (Subrayan et al. 2025).

0.0166

0.0207

0.090

9

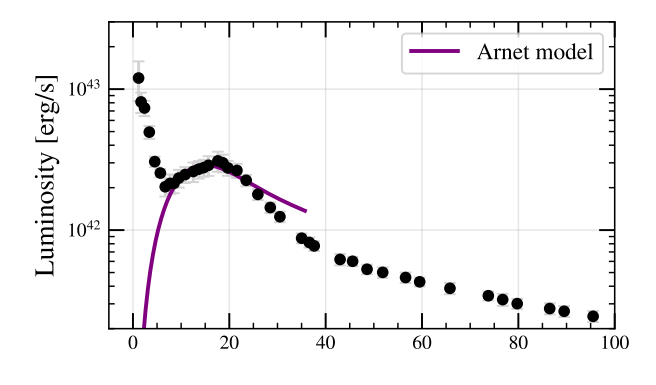
10

As the V-band light curve reaches its secondary peak at around day 20, the B-V and g-r colors of SN 2024iss display another redward evolution until reaching the reddest colors of $\sim 1.29 \pm 0.37$ and 0.97 ± 0.37 magnitudes, respectively, at $t \approx 40$ days. Overall, such color evolution is broadly consistent with those of other SNe IIb, with the exception of SN 2011dh, which does not show a clear initial rapid reddening phase and only exhibits a very shallow initial decline in the V band (Tsvetkov et al. 2012) and P48 g band (Arcavi et al. 2011).

3.3. Pseudo-bolometric Luminosity and Temperature Evolution

Using extinction-corrected photometry, we constructed the pseudo-bolometric light curve of SN 2024iss with the Light Curve Fitting package (Hosseinzadeh & Gomez 2020). The SED at each epoch was fitted with a blackbody function, employing a Markov Chain Monte Carlo (MCMC) routine with the emcee package (Foreman-Mackey et al. 2013). We also included the NIR photometry published in Yamanaka et al. (2025), as the NIR contribution at later phase at a few months after the explosion may reach up to $\sim\!35\%$ (Medler et al. 2022). Temporal evolutions of the constructed pseudo-bolometric luminosity, the blackbody temperature, and the radius of SN 2024iss are shown in Figure 4. The latter two parameters were derived by fitting a blackbody spectrum to the SED constructed from the UV, optical, and NIR (uvw2, uvm2, uvw1, B, V, g, r, i, J, H, and K-band) photometry.

As shown in the top panel of Figure 4, the maximum pseudo-bolometric luminosity of SN 2024iss yields $L = (1.2 \pm 0.4) \times 10^{43} \text{erg s}^{-1}$, which is observed on day 1.2. Owing to the lack of multiband photometry at even earlier phases, the constructed pseudo-bolometric light curve does not cover the phase before day 1.2. The pseudo-bolometric light curve subsequently declines until reaching a turning point on day 6.7. The light curve then rises again until a secondary peak of $L = 3.1 \times 10^{42} \text{erg s}^{-1}$, $log(L/\text{erg s}^{-1}) = 42.49 \pm 0.07$ is attained on day 17.6, which is



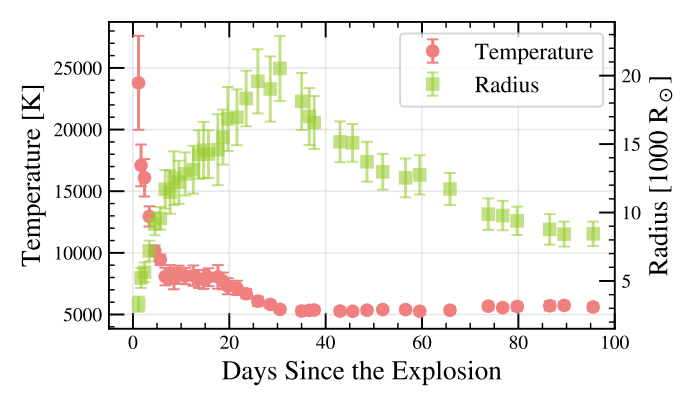


Fig. 4: Top: Pseudo-bolometric light curve of SN 2024iss. The purple line shows the best-fit Arnett model to the secondary peak. Bottom: Evolution of the blackbody temperature and the photospheric radius of SN 2024iss, as indicated by the left- and right-hand ordinates, respectively.

coincident with the time of the V-band maximum. The pseudobolometric luminosity of SN 2024iss observed at its secondary peak is slightly above the mean peak luminosity of SNe IIb given by Prentice et al. (2016), namely $log(L/\text{erg s}^{-1}) = 42.36 \pm 0.26 \\ 0.11$. This may result from either a larger amount of 56 Ni synthesized during the SN explosion or a more thorough mixing of 56 Ni throughout the ejecta (Liu et al. 2025).

Both the temperature and photospheric radius of SN 2024iss show similar evolution to those of other SESNe (Taddia et al. 2018). The effective temperature drops rapidly during the early phase, from $\sim 23,000$ K to $\sim 8,200$ K within the first ~ 7 days, until entering a plateau phase. It remains constant until $t \approx 18$ days and then decreases, which is roughly coincident with the V-band maximum light. The temperature evolution of SN 2024iss derived by fitting a blackbody to the SED mirrors the trend observed in the B-V and g-r color curves (see, Section 3.2 and Figure 3).

3.4. Estimating the ⁵⁶Ni Mass

We fit the second peak of the bolometric light curve with the Arnett law, which was first proposed as an oversimplified expanding fireball model to explain the early light curve of Type Ia supernovae (SNe Ia) by Arnett (1982). Valenti et al. (2008) extended this model to SESNe by separating their photometric evolution into the photospheric and nebular phases, and introducing a γ -ray leakage term. This model involves two key

parameters to describe the secondary peak of the bolometric light curve, namely the synthesized nickel mass in the SN ejecta $(M_{\rm Ni})$, which determines the peak bolometric luminosity, and the ejecta mass $(M_{\rm ej})$, which is related to the photon diffusion time τ_m and the width of the bolometric light curve. According to Arnett (1982), τ_m can be expressed in terms of $M_{\rm ej}$ and the photospheric velocity $v_{\rm ph}$:

$$\tau_m = \sqrt{2} \left(\frac{\kappa_{\text{opt}}}{\beta c} \right)^{1/2} \left(\frac{M_{\text{ej}}}{\nu_{\text{ph}}} \right)^{1/2} \tag{1}$$

where $\beta \approx 13.8$ is a constant, c denotes the speed of light and $v_{\rm ph}$ is the photospheric velocity. Following common assumptions for SESNe (Taddia et al. 2018; Dong et al. 2024), we adopt a constant optical opacity $\kappa_{\rm opt} = 0.07~{\rm cm^2~g^{-1}}$ and a γ -ray opacity $\kappa_{\gamma} = 0.027~{\rm cm^2~g^{-1}}$. This model assumes all ⁵⁶Ni is placed at the center of the SN ejecta without any outward mixing, and that the opacity remains constant throughout the evolution. For a spherical SN ejecta, $v_{\rm ph}$ is linked to the kinetic energy and $M_{\rm ej}$ through the relation:

$$E_k \approx \frac{3}{5} \frac{M_{\rm ej} v_{\rm ph}^2}{2} \tag{2}$$

Following the prescriptions described by Dessart & Hillier (2005), we adopt a photospheric velocity of 7500 km s⁻¹, as measured from absorption minimum of the Fe II λ 5169 in the near-maximum-light spectrum. This velocity is comparable to those of SN 1993J (8000 km s⁻¹) and other SNe IIb(Medler et al. 2022), but is significantly lower than the velocity measured from the H α P Cygni profile in the spectrum of SN 2024iss, which is 15,000 km s⁻¹ (Yamanaka et al. 2025).

We fit the bolometric light curve of SN 2024iss spanning the phase from $t \approx +7$ to +30 days with the emcee package (Foreman-Mackey et al. 2013). The time interval was chosen to encompass the secondary peak but exclude the nebular phase when the observed flux becomes dominated by various emission lines from iron-group elements. The best-fit result is shown by the purple line in the upper panel of Fig. 4, indicating $M_{\rm Ni} = 0.117 \pm 0.013 \ M_{\odot}, \ M_{\rm ej} = 1.272 \pm 0.343 \ M_{\odot}$ and $E_k = 0.427 \pm 0.115 \times 10^{51}$ erg. The nickel mass derived for SN 2024iss is similar to those reported for other Type IIb SNe, for example, 0.11 M_{\odot} for SN 2013df (Morales-Garoffolo et al. 2014). However, the ejecta mass of SN 2024iss appears to be lower than all of the SN IIb sample presented in Medler et al. (2021). Additionally, we measure the magnitude decline from maximum light to 15 days after that in the V-band light curve, i.e., $\Delta m_{15}(V) = 1.13$ mag, which is larger compared to an average value of 0.93 mag derived for a sample of Type IIb SNe (Taddia et al. 2018). Such a rapid decline may not solely result from a low ejecta mass, but may also be caused by other effects such as vigorous mixing of radioactive ⁵⁶Ni throughout the SN ejecta, or variations in the density profile of the ejecta (Liu et al. 2025). A more detailed analysis will be discussed in Section 7.3.

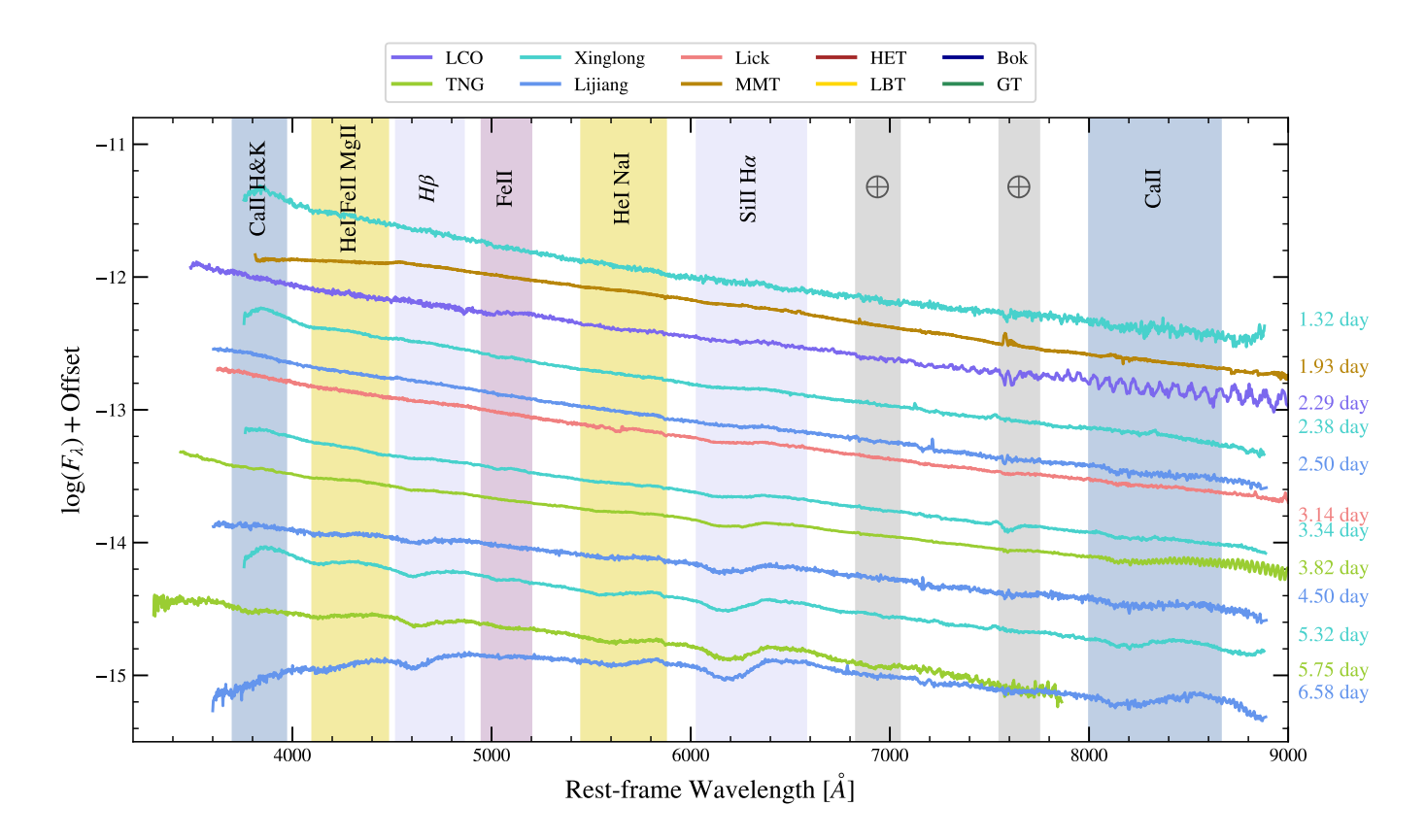


Fig. 5: Spectral sequence of SN 2024iss, spanning the first 7 days after the explosion. Phases are marked on the right. Different colors distinguish the different spectrographs used in the observations, as shown at the top. A log of the spectroscopy of SN 2024iss is given in Table A.3.

4. Optical Spectroscopy

4.1. Spectral evolution

We collected a total of 51 spectra of SN 2024iss, spanning the phases from $t \approx +1.3$ to +87.0 days. We present the spectral sequences before and after $t \approx 7.0$ days in Figures 5 and 6, respectively. All spectra were corrected for the Galactic reddening and are shown in the rest frame. Within the first 7 days after the estimated explosion, the spectra of SN 2024iss are characterized by blue and featureless continuums. At this stage, the SN emission is dominated by the shock cooling. The outermost envelope of the exploding progenitor star manifests sufficiently high temperature at the location of the photosphere, where the high-opacity line-forming regions were not often present. We see no narrow emission features in the first few spectra of SN 2024iss, as shown in Figure 5. However, narrow emission features can be identified in the spectra of SN 1993J (Benetti et al. 1994) and 2013cu (Gal-Yam 2017) within the first days after the explosion.

The absence of such narrow lines may indicate either a relatively low density or less radially extended CSM content around the progenitor of SN 2024iss. As the ejecta cool down, the characteristic P Cygni profiles of the Balmer lines start to emerge in the $t \approx 3.8$ day spectrum. Features of He I $\lambda 5876$, H_{γ} and Ca II NIR $\lambda\lambda 8498$, 8542, 8662 can be also identified in the spectra starting from $t \approx 5.3$ days.

As illustrated in Figure 6, the spectroscopic evolution of SN 2024iss after the shock-cooling phase show close

resembles to those of other SNe IIb (Filippenko 1997; Morales-Garoffolo et al. 2014; Medler et al. 2022). All spectrum are normalized by the fitted blackbody continuum. After $t \approx 18.4$ days, Fe II lines develop P Cygni profiles. Meanwhile, He I $\lambda 5876$, 6678 features become progressively prominent after the shock cooling. We attribute the absorption troughs at $\sim 4300 \,\text{Å}$ to the blending of several lines, namely He I $\lambda 4472$, Mg I $\lambda 4481$ and Fe II $\lambda 4549$, consistent with the line identification in the literature (e.g., Hachinger et al. 2012; Silverman et al. 2009; Morales-Garoffolo et al. 2014).

Before entering the nebular phase, the Ca II H&K $\lambda\lambda 3943$, 3969 and Ca II $\lambda\lambda 8498$, 8542, 8662 lines manifest as prominent blue-shifted absorption features. As the ejecta cool, the [Ca II] $\lambda\lambda 7291$, 7323 doublet appear around day 32, followed by a series of oxygen lines, i.e., [O I] $\lambda\lambda 6300$, 6364 and O I $\lambda 7774$. Such signatures can be clearly identified in the $t\approx 61$ day spectrum. By $t\approx 87$ days, as the ejecta cool, various forbidden lines become prominent in the spectrum, i.e., double peak in the Ca II $\lambda\lambda 8498$, 8542, 8662 feature (see further discussions in Section 4.3).

4.2. Velocity evolution

The photospheric velocities of SN 2024iss as measured from H_{α} , H_{β} , H_{γ} , He I λ 5876, He I λ 6678, Fe II λ 5018, Fe II λ 5169, Ca II H&K $\lambda\lambda$ 3943, 3969 and Ca II $\lambda\lambda$ 8498, 8542, 8662 lines are shown in Figure 7. For each spectral feature that shows a P Cygni

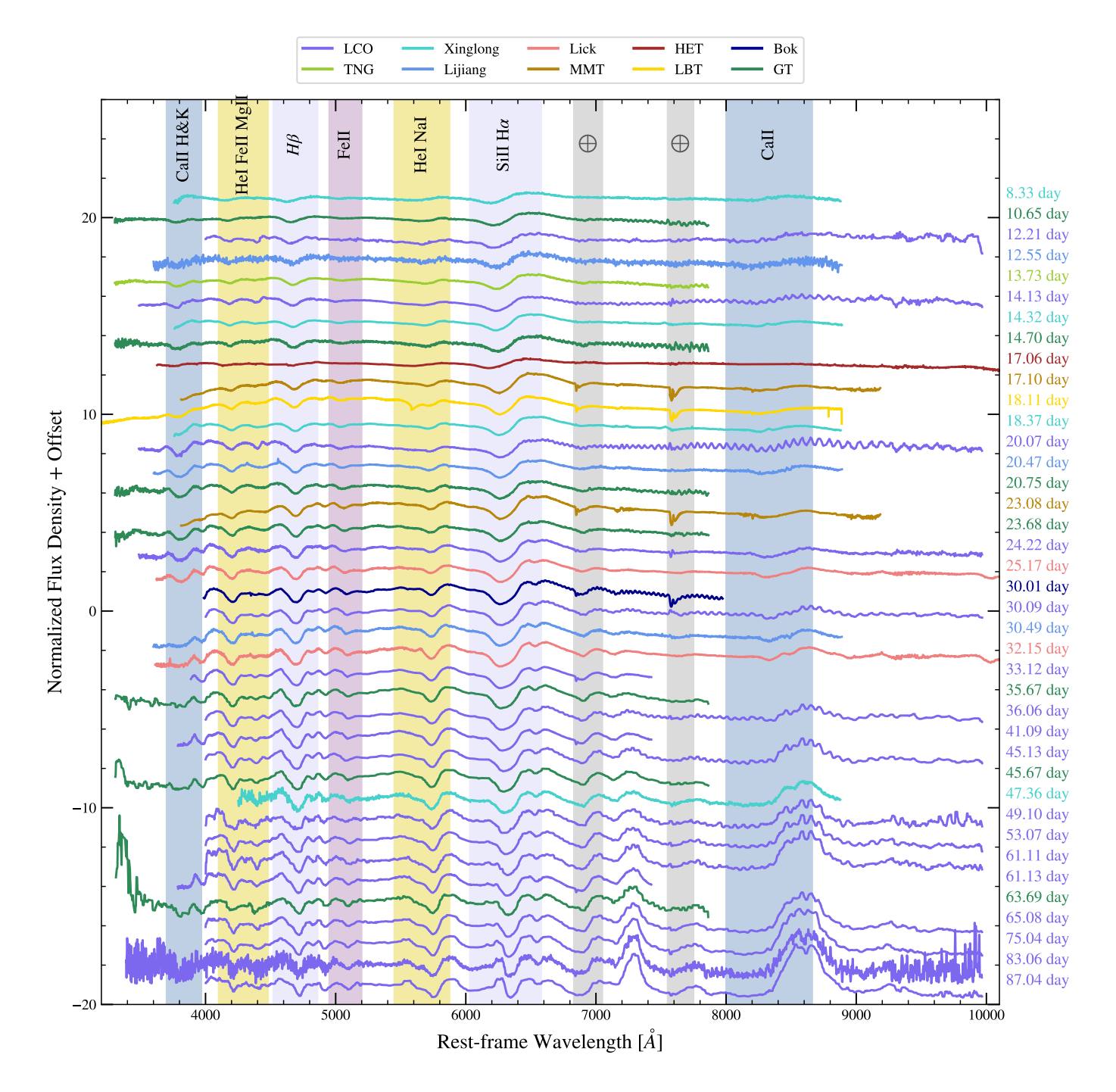


Fig. 6: Spectral consequence of SN 2024iss obtained during the phase from $t \approx 8$ to 87 days after the explosion. The layout of the figure is similar to those of Figure 5. For the purpose of presentation, the best-fit blackbody function was subtracted from each spectrum. A log of the spectroscopy of SN 2024iss is presented in Table A.3.

profile, we subtracted the pseudo-continuum and fitted the residual with a Gaussian function. We then inferred the expansion velocity from the blueshifted absorption minimum. After the V-band maximum, velocities inferred from the Balmer lines and the He I $\lambda 5876$ feature show a slower decline, which may be due to the transition of energy source from adiabatic to radiative cooling. The Balmer lines shows a similar velocity evolution, with velocities consistently higher than those of other lines. Additionally, Ca II lines also exhibit relatively high expansion velocities, possibly due to element mixing (Fransson & Chevalier

1989). At t> 25 days, measuring Ca II velocity is difficult because of emission-dominated profiles. The Fe II $\lambda 5169$ line velocities are key tracers of the receding photosphere in the expanding ejecta (Dessart & Hillier 2005). We measure a velocity of $\sim 7500 \pm 500 \, \mathrm{km \, s^{-1}}$ from the Fe II $\lambda 5169$ line at around the V-band peak of SN 2024iss. We also note that the P Cygni profile of the Fe II $\lambda 5169$ feature suffered from increased contamination as other lines emerge, introducing larger uncertainties in profile fitting and velocity estimation. In Figure 8 we compare the velocity evolution of SN 2024iss with that of other SNe IIb.

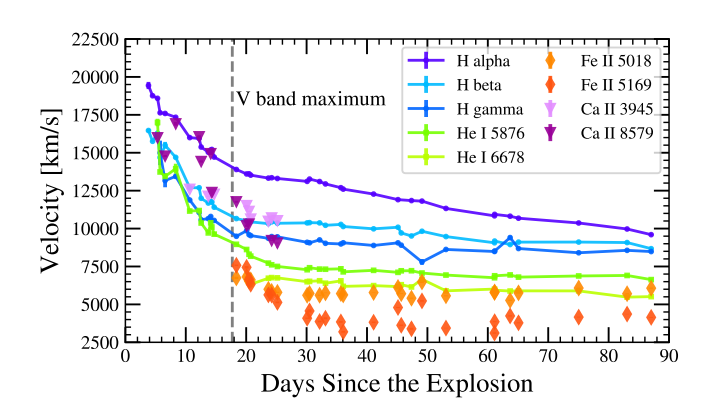


Fig. 7: Evolution of the expansion velocity of SN 2024iss measured from spectral features of H_{α} , H_{β} , H_{γ} , He I, Fe II and Ca II. The vertical gray-dashed line marks the epoch of *V*-band light curve peak. Photospheric velocities, inferred from the absorption minima of Balmer and He I λ 5876 lines, appear to be faster than other spectral features.

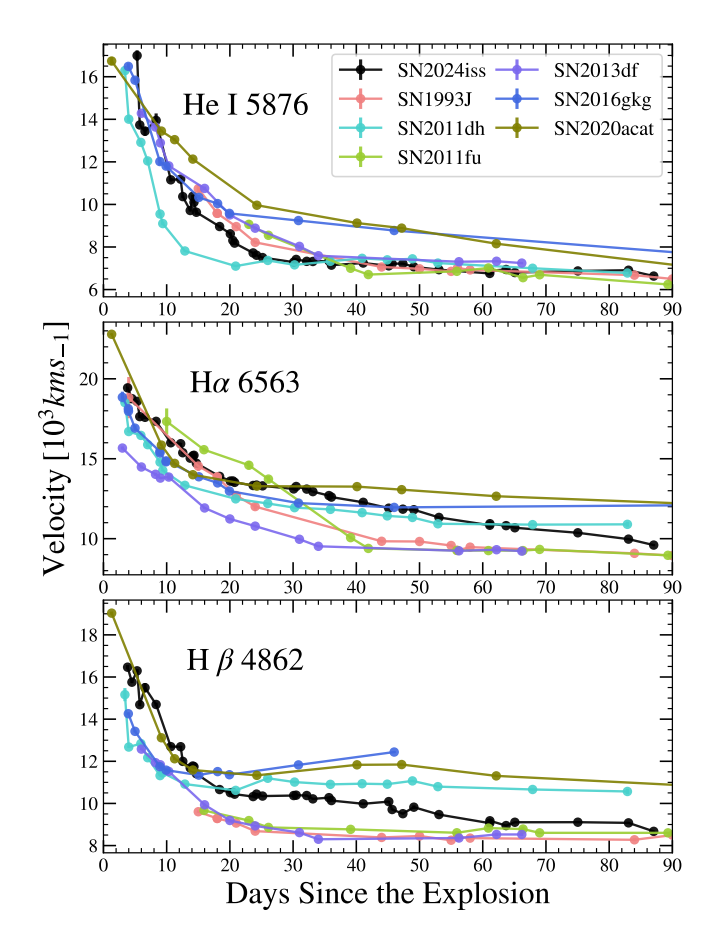


Fig. 8: Temporal evolution of He I λ 5876, H $_{\alpha}$ and H $_{\beta}$ of SN 2024iss compared to that measured for SNe 1993J, 2011dh, 2011fu, 2013df, 2016gkg and 2020acat.

4.3. Comparison with Other Type IIb SNe

Figure 9 compares the spectra of SN 2024iss with those of SNe 1993J (Barbon et al. 1995; Matheson et al. 2000), 2011dh (Arcavi et al. 2011; Ergon et al. 2014), 2011fu (Kumar et al.

2013; Morales-Garoffolo et al. 2015; Shivvers et al. 2019), 2013df (Szalai et al. 2016; Shivvers et al. 2019), 2016gkg (Kilpatrick et al. 2017) and 2020acat (Medler et al. 2022) at similar phases. All comparison spectra were downloaded from the WISEREP⁸ (Yaron & Gal-Yam 2012) and have been corrected for the redshifts of the host galaxies and the reported reddenings. Basic information of the comparison SNe is compiled in Table 3.

At early phases, SNe 2024iss and 1993J exhibit similar H_{α} and H_{β} profiles, while SN 1993J displays a more prominent He I λ 5876. The Ca II NIR triplet profile of SN 2024iss shows a striking resemblance to that of SN 2020acat. Additionally, we note that among all the spectra of SNe IIb compared in Fig. 9 (a), SNe 2011dh and 2011fu exhibit more prominent line profiles at about ten days before V-band maximum, indicating a prompt spectral evolution.

At around the *V*-band maximum, as shown in Fig. 9 (b), both SNe 2024iss and 1993J exhibit a flat-topped emission component of H α , which may likely be caused by the strengthening He I λ 6678. In contrast, SN 2013df displays a single-peaked H α emission, while SNe 2011dh and 2011fu exhibit double-peaked profiles, likely indicating a rather prompt mixing of helium into the H-rich envelope. SN 2011fu shows the most prominent He I λ 5876 feature among the sample. Additionally, SNe 2024iss and 2013df are characterized by shallower Ca II $\lambda\lambda$ 8498, 8542, 8662 absorptions relative to other comparison SNe. We also note that both SNe 2024iss and 1993J display a double-peaked feature near 4000 Å, whereas SNe 2011fu and 2016gkg show a single Ca II H&K $\lambda\lambda$ 3943, 3969 emission peak. Finally, SN 2024iss shows a single-peaked line near 4800 Å which can be attributed to H β , where other comparison SNe display line complexes.

In Fig. 9 (c) we compare the spectrum of SN 2024iss at ~ 31 days after the V-band peak to those of other comparison SNe at a similar phase. SN 2024iss exhibits broader Ca II $\lambda\lambda$ 8498, 8542, 8662 absorption in comparison with other SNe. Furthermore, unlike the significantly weakened H α absorption component observed in SNe 1993J and 2013df, such a feature still remains prominent in SNe 2024iss, 2016gkg, and 2020acat.

At $t \approx 67$ days after the V-band maximum light, as shown in Fig. 9 (d), the iron features became more prominent, indicating a transition to the nebular phase, when the continuum spectral emission becomes dominated by a blend of Fe-group features. The strength of the Balmer lines are decreasing while several He I lines remain strong, highlighting the type IIb nature of the SN. Additionally, the spectrum of SN 2024iss exhibits a doublepeaked Ca II λλ8498, 8542, 8662 profile. Among the comparison sample, only SN 1993J shows a similar feature at a similar phase. At earlier phases, these lines are blended due to line broadening. As the ejecta cool down, individual components separate and become distinguishable. The evolution of the double-peaked Ca II NIR profile of SN 2024iss during the nebular phase remains an intriguing question. Additionally, similar to SNe 1993J and 2013df, SN 2024iss still shows H α at this phase, which was no longer identified in the spectra of SN 2011fe, 2011dh, and 2020acat obtained at a similar epoch. The presence of hydrogen at this phase suggests elemental mixing or a relatively massive hydrogen envelope. Finally, we note that SN 2024iss also shows

⁸ https://www.wiserep.org

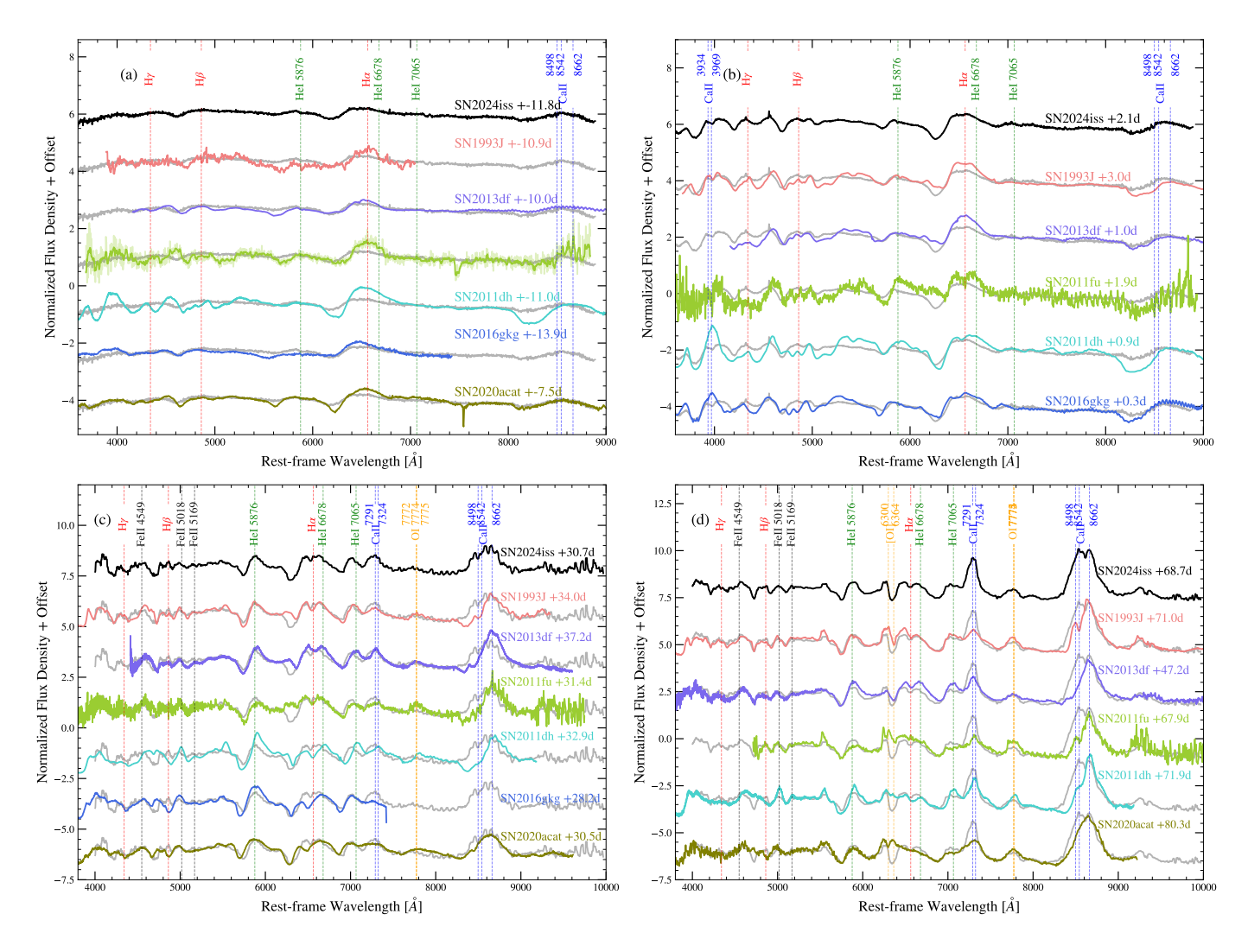


Fig. 9: Spectra of SN 2024iss at -12(a), 2(b), 31(c), and 69(d) days relative to the *V*-band light-curve peak, compared to other well-studied SNe IIb at similar phases. Phases with respect to the *V*-band maximum are labeled. All spectra are shown in the rest-frame and normalized. The vertical dashed lines mark the positions of certain spectral features at zero rest-frame velocity. For comparison, the gray curve underlying the spectrum of each comparison SN shows the shifted spectrum of SN 2024iss that matches their mean flux within the displayed wavelength range.

the strongest [Ca II] $\lambda\lambda7291$, 7323 emission feature relative to the comparison SNe.

5. Shock-Cooling Model Fitting

Among various models developed to describe the shock cooling emission, we adopt the one by Sapir & Waxman (2017) (hereafter SW17) to fit the multiband light curves of SN 2024iss up to $t \approx 5$ days after the explosion. The key parameters in SW17 include the envelope radius (R), the envelope mass ($M_{\rm env}$), the shock velocity ($v_{s,8.5}$), the product of stellar mass and a numerical factor related to envelope structure ($f_{\rho}M$) and the first-light time (t_0).

SW17 assumes a polytropic density profile, where polytropic index n=3/2 corresponds to the case of RSGs with convective envelope and n=3 corresponds to the case of BGSs with radiative envelope. Building on the framework of Rabinak & Waxman (2011), SW17 introduced an exponential suppression factor in luminosity. This modification extends the

validity of the model to a few days after the explosion. According to the different polytropic index (n = 3/2[3]), the bolometric luminosity is given by (following the formulation recast by Arcavi et al. (2017)):

$$L_{\text{RW}} = 2.0[2.1] \times 10^{42}$$

$$\times \left[\frac{v_{s,8.5}t^2}{f_0 M \kappa_{0.34}} \right]^{-0.086[-0.175]} \frac{v_{s,8.5}^2 R_{13}}{\kappa_{0.34}} \text{ erg s}^{-1}$$
 (3)

$$L/L_{\text{RW}} = 0.94[0.79] \times$$

$$\exp\left[-\left(\frac{1.67[4.57]t}{(19.5\kappa_{0.34}M_e v_{-0.5}^{-1.5})^{0.5}}\right)^{0.8[0.73]}\right] \quad (4)$$

where t is time since explosion in days, $v_{s,8.5}$ is shock velocity in $10^{8.5}$ cm s⁻¹, R_{13} is envelope radius in 10^{13} cm, $\kappa_{0.34}$ is opacity in 0.34 cm²g⁻¹, M is ejecta mass (core mass M_c + envelope mass

 M_e) in solar masses, and when $R_c/R \ll 1$, f_ρ can be approximated as:

$$f_{\rho} \approx \begin{cases} (M_e/M_c)^{0.5}, n = 3/2\\ 0.08(M_e/M_c), n = 3 \end{cases}$$
 (5)

The temporal evolution of the color temperature is given as:

 $T = 2.05[1.96] \times 10^4$

$$\times \left[\frac{v_{s,8.5}^2 t^2}{f_o M \kappa_{0.34}} \right]^{0.027[0.016]} \left(\frac{R_{13}}{\kappa_{0.34}} \right)^{0.25} t^{-0.5} K \quad (6)$$

Assuming that the continuum emission of SN 2024iss can be well approximated by a blackbody spectrum, we can calculate the photospheric radius from the Stefan-Boltzmann law and fit the model to the multiband photometry. We fit the swift UVOT uvw2, uvm2, uvw1, B, V, g, r and i-band light curves of SN 2024iss with the open-source package Light Curve Fitting (Hosseinzadeh & Gomez 2020), implementing the analytic expression given by SW17, with an index n = 3/2. We restrict the fit to data obtained within five days after the estimated time of explosion, as beyond this point the energy input from the radioactive decay of ⁵⁶Ni exceeds 30% (see Section 3.4), and therefore biases the results. Within 5 days after explosion, the blackbody temperature satisfies the criterion $T > 0.7 \,\mathrm{eV}$, ensuring the validity of the SW17 model during the period. The fit was performed using a Markov Chain Monte Carlo (MCMC) routine with 30 walkers and 2000 steps (1000 steps for burn-in). The additional scatter term (σ) was included to account for intrinsic variability and deviations from the blackbody assumption.

The MCMC parameters distributions and the best-fit model multiband light curves are presented in Figure 10. The parameters that best describe the shock-cooling phase are the following: R = 244 ± 43 R_{\odot} , $M_{\rm env}$ = 0.11 ± 0.04 M_{\odot} , $v_{s,8.5}$ = (1.9 ± 0.3) × $10^{8.5}$ cm s⁻¹, $f_{\rho}M$ = 100 ± 65 M_{\odot} and $t_{\rm exp}$ = 60442.41 ± 0.05 d. The model light curves agree fairly well with the observations. The inferred envelope mass and radius of SN 2024iss are larger than that of SN 2016gkg (i.e., ~0.03 M_{\odot} , ~141 R_{\odot} ; Piro et al. 2021), indicating a more extended envelope than Type cIIb SNe. The envelope mass of SN 2024iss is lower than that of SN 1993J (~0.2 M_{\odot} ; Woosley et al. 1994), suggesting that its envelope is less extended than some Type eIIb SNe.

6. X-ray Constraints on the Circumstellar Medium

Figure 11 shows the unabsorbed 3–10 keV X-ray luminosity of SN 2024iss. The errors were estimated by adding the uncertainties in the X-ray photometry and the distance modulus in quadrature. As the temperature of post-shock gas is higher than 2×10^7 K, thermal bremsstrahlung emission in the forward shock dominates over the cooling (Fransson et al. 1996; Chevalier & Fransson 2017). Assuming a homogeneous wind with $v_{\rm wind} = 10\,{\rm km\,s^{-1}}$ according to Fransson et al. (1996), our best-fit result is consistent with a mass-loss rate of $\dot{M} = 1.6 \times 10^{-5}\,M_\odot\,{\rm yr^{-1}}$ and a shock velocity of $v_s^{\rm X-ray} \approx 9.5 \times 10^8\,{\rm cm\,s^{-1}}$. Based on the 3σ and 5σ confidence intervals of the 3–10 keV luminosity as indicated by the green and purple shaded regions in Fig. 11, the mass-loss rate is constrained as $1.2-1.9 \times 10^{-5}$

and $1.0-2.2 \times 10^{-5} \ M_{\odot} \ \rm yr^{-1}$, respectively. The mass loss rate inferred for the X-ray observations of SN 2024iss is comparable to those of SNe 1993J (i.e., $4\times 10^{-5} \ M_{\odot} \ \rm yr^{-1}$, Fransson et al. 1996) and 2013df (i.e., $8\times 10^{-5} \ M_{\odot} \ \rm yr^{-1}$, Kamble et al. 2016). The shock velocity inferred from the X-ray light curve of SN 2024iss is consistent with that estimated by the shock-cooling model as discussed in Section 5, namely $v_s = (6.0 \pm 0.9) \times 10^8 \ \rm cm \ s^{-1}$, but is much smaller than the result inferred from the early time H_{α} velocity (i.e., $v_{H_{\alpha}} = 1.94 \times 10^9 \ \rm cm \ s^{-1}$).

To further investigate the CSM properties, we also used the method of emission measure (EM) to constrain the density structure of the CSM:

$$EM = \int n_e n_H dV \approx \frac{\rho(r)^2 V_{\text{CSM}}}{\mu_e \mu_H m_p} \tag{7}$$

where $\rho(r)$ represents the mass density of the CSM at radius $r, V_{\rm CSM} \approx 4\pi r^2 \Delta r$ is the volume of the shocked CSM shell, with $\Delta r \approx 0.1 r$ denoting the thickness of the forward-shocked CSM. We adopt a mean molecular weight of $\mu=0.61$ for the ionized CSM with solar metallicity, where $\mu_e \approx 1.3$ and $\mu_H \approx 1.15$. The EM parameter can be derived from the "Norm" column in Table A.2.

Figure 12 shows the radial density profile of the CSM around SN 2024iss (ρ_{CSM}) as inferred from the EM method, together with that of the homogeneous wind with different mass-loss rates. The former lies between the 10^{-5} and $10^{-4} M_{\odot} \text{ yr}^{-1}$ curves of steady mass loss, with a mean value of $(5.55 \pm 1.57) \times$ $10^{-5} M_{\odot} \text{ yr}^{-1}$. This estimate is higher than the value derived from the X-ray light curve of SN 2024iss. However, it is comparable to the mass loss rate of $8 \times 10^{-5} \,\mathrm{M}_{\odot} \,\mathrm{yr}^{-1}$ estimated for SN 2013df, assuming a wind velocity of $10 \,\mathrm{km}\,\mathrm{s}^{-1}$ (Kamble et al. 2016). The discrepancy may be due to the unusually low intrinsic neutral hydrogen column density of SN 2024iss, namely $N_{\rm H}$ $< 8 \times 10^{19} \ cm^{-2}$ after subtracting the Galactic contribution. The low column density would introduce a degeneracy in the X-ray spectral fitting and thus overestimate the mass-loss rate compared to the free-free emission model. A power-law fit to this profile yields $\rho_{\rm CSM} \propto R^{-2.19\pm0.10}$, which is nearly consistent with the canonical R^{-2} expected for a steady wind.

We also note that the inferred $N_{\rm H}$ at t ~1.6 days after the SN explosion exhibited a low value of ~ $9 \times 10^{19} \, \rm cm^{-2}$, which is equal to the combined value of the Galactic and the SN host. The negligible absorption from the CSM may indicate that the forward shock has already traversed the entire CSM at this phase. Assuming a constant shock velocity of $v_{\rm sh} \approx 10^9 \, \rm cm \, s^{-1}$, we infer that the CSM was confined within a radius of $R \lesssim 1.3 \times 10^{14} \, \rm cm$. With a wind velocity of $10 \, \rm km \, s^{-1}$, the rather compact CSM suggests that the progenitor had experienced significant mass ejection roughly four years before the explosion.

In Figure 13, we compare the 0.3–10 Kev X-ray luminosity evolution of SN 2024iss with those of several other Type IIb SNe, including SNe 1993J (Chandra et al. 2009), 2011dh (Soderberg et al. 2012), 2013df (Kamble et al. 2016), 2016gkg (Dwarkadas 2025) and 2024abfo (Reguitti et al. 2025). The X-ray luminosity of SNe 1993J and 2013df were estimated in 0.3–8 keV band. The uncertainty introduced from different band can be neglected, as the X-ray emission contributes little above 8 keV. Among the comparison sample, SN 1993J is found to fol-

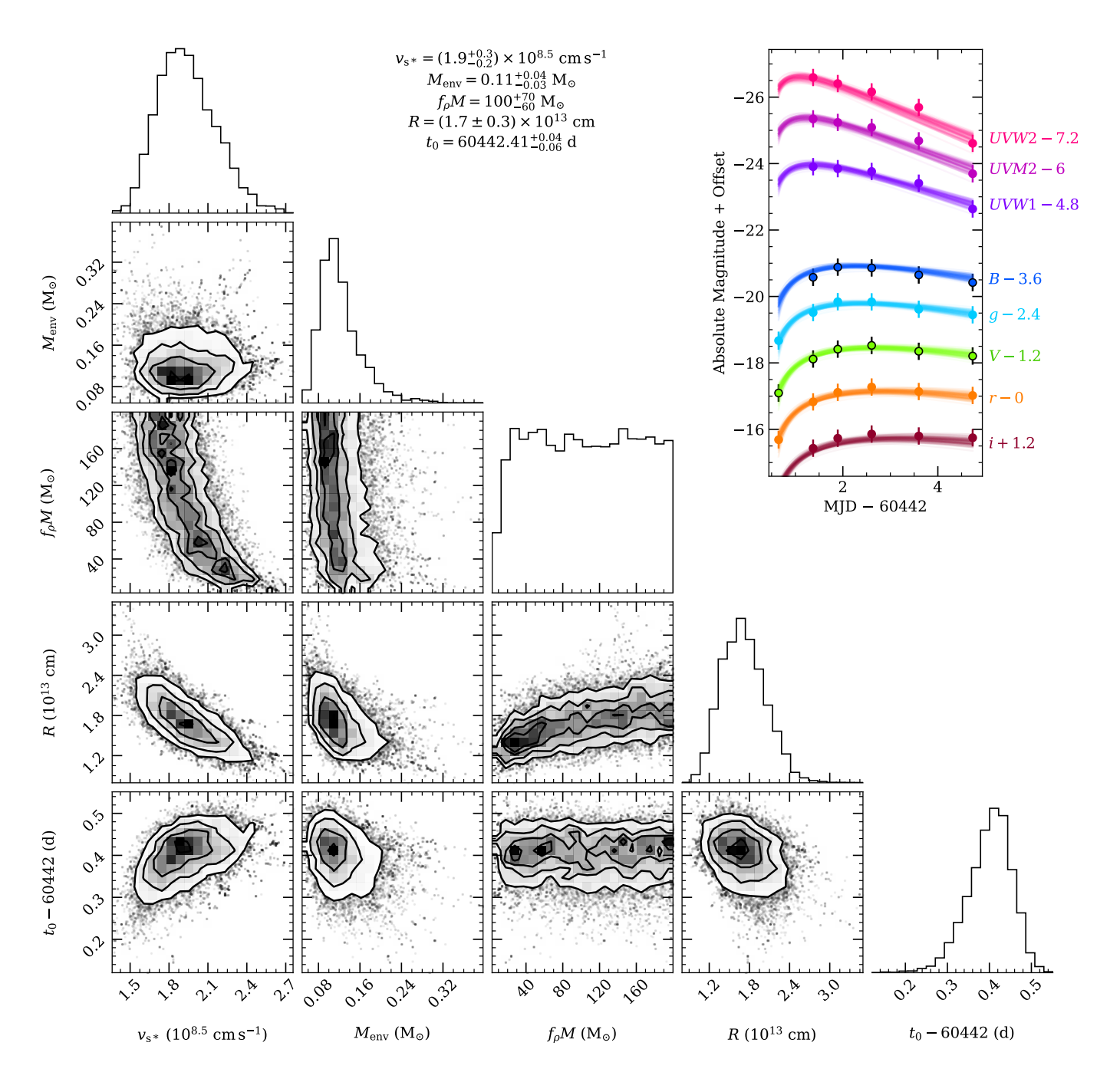


Fig. 10: The Corner plot that presents the posterior distributions of the SW17 shock-cooling light-curve model of SN 2024iss. The fit to the early light curves was restricted to five days after the estimated time of the SN explosion. The best-fit parameters are listed at the top of the figure. The upper-right inset presents the model light curves that best fit the multiband photometry, as displayed by color-coded curves and symbols, respectively.

low a power-law decline with an index of ~ -0.68 (see the black dashed line in Figure 13). While SN 2024iss, SN 1993J, and SN 2016gkg exhibit an overall higher X-ray luminosity in comparison with SN 2011dh and SN 2024abfo.

The high X-ray luminosity of the former three events can be attributed to an extended hydrogen-rich envelope and dense wind-like CSM (Kamble et al. 2016). In contrast, those Type IIb SNe that are faint in X-ray band may arise from more compact progenitors with a weaker ejecta-CSM interaction. Follow-

ing the framework of Chevalier & Soderberg (2010), we classify SN 2024iss as Type eIIb, which is compatible with its double-peaked optical light curve and high mass-loss rate, as observed in SNe 1993J, 2013df and 2011hs.

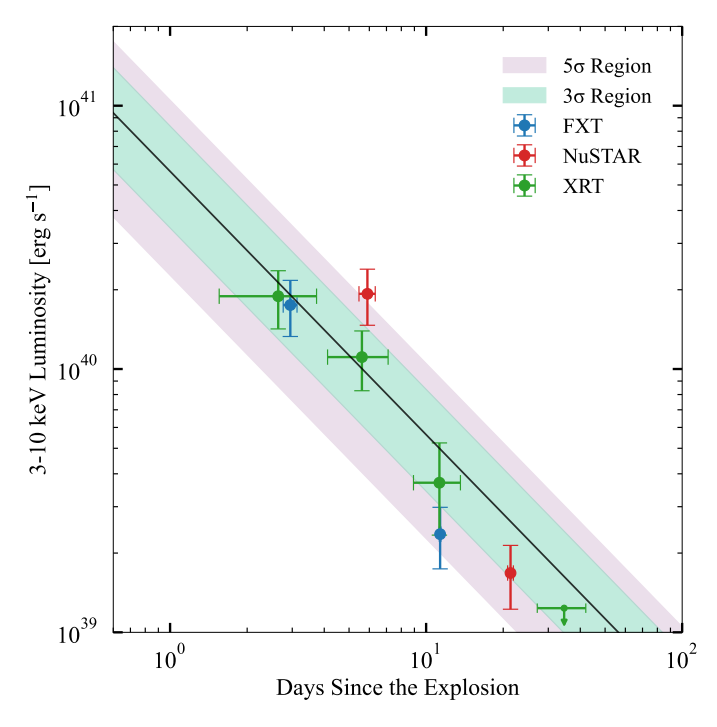


Fig. 11: The unabsorbed X-ray luminosity of SN 2024iss observed in the 3–10 keV band. The red, green, and blue data points represent the observations conducted with the NuSTAR, Swift-XRT, and EP-FXT, respectively. The black line shows the best-fit thermal bremsstrahlung model, with a mass-loss rate of $1.6 \times 10^{-5}~M_{\odot}~\rm yr^{-1}$ and a shock velocity of $9.5 \times 10^8~\rm cm~s^{-1}$. The green and purple shaded areas indicate the $3-\sigma$ and $5-\sigma$ confidence regions, respectively.

7. Discussions

7.1. The progenitor of SN 2024iss

The best fit to the Arnett model based on the second light curve peak of SN 2024iss suggests an ejecta mass of $M_{\rm ej} = 1.27 \pm$ $0.34\,M_{\odot}$ (see Section 3.4). Assuming a typical mass for the neutron star remnant of $1.4 M_{\odot}$ (Thorsett & Chakrabarty 1999), we estimate a helium core mass of $M_{remnant} + M_{ej} + M_{env} = 2.8 M_{\odot}$. Using the progenitor grid of Sukhbold et al. (2016), this indicates a main-sequence mass of $M_{ZAMS} = 9 - 11 M_{\odot}$, which is similar to that inferred for SN 2016gkg (Kilpatrick et al. 2022) and compatible with the predicted mass range of Type IIb progenitors in a binary system (Yoon et al. 2017). By fitting the first peak in the optical light curves with the shock-cooling model presented by P21, we infer that the mass and radius of the hydrogen envelope of SN 2024iss are $M_{\rm env} = 0.11 \pm 0.04 \, \rm M_{\odot}$ and $R_{\rm env} = 224 \pm 43 \, {\rm R}_{\odot}$ (see Section 5). The inferred mass and radius favors for a YSG progenitor star. In contrast, models involving single Wolf-Rayet stars are not able to produce an ejecta mass lower than 5 M_{\odot} (Lyman et al. 2016). A binary system may naturally account for the partially depleted hydrogen envelope required for the progenitor of SN 2024iss.

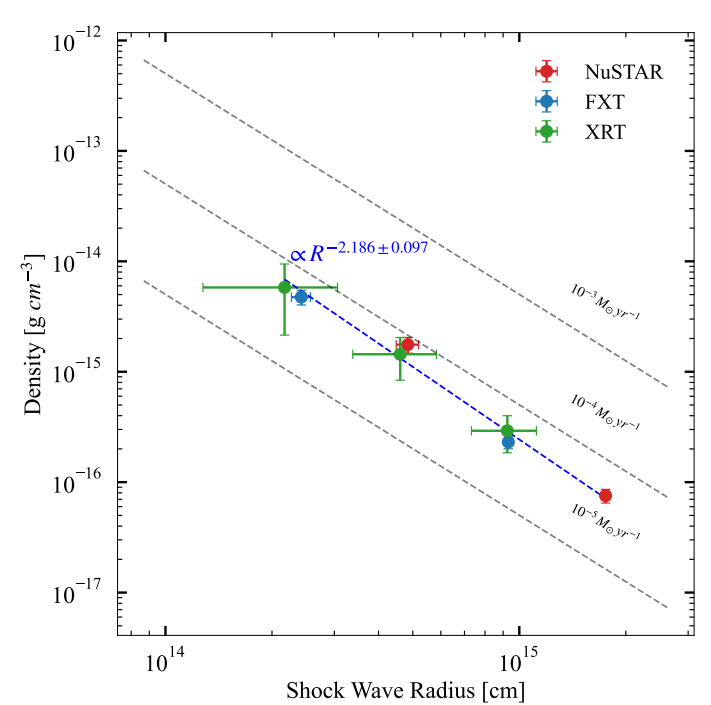


Fig. 12: The CSM density profile as inferred from the emission measure. Data from NuSTAR, Swift-XRT, and EP-FXT are indicated by the red, green, and blue circles, respectively. The gray dashed lines represent the wind-like density profiles corresponding to mass-loss rates of $\dot{M}=10^{-5},\ 10^{-4},\ 10^{-3}\ M_{\odot}\ \rm yr^{-1}$. The blue dashed line denotes the power-law fit to the X-ray light curve. The inferred radial density profile $\rho_{\rm CSM} \propto R^{-2.19}$ is incompatible with a homogeneous mass-loss wind.

7.2. SN 2024iss: Bridging the Gap Between subclasses of Type ellb and Type cllb

Note that in the classification scheme of Yoon et al. (2017), the envelope mass of SN 2024iss is close to the threshold of 0.15 M_☉ adopted to distinguish between Types eIIb and cIIb. For comparison, the compact Type IIb SN 2016gkg has an envelope mass of $\sim 0.03 \, \mathrm{M}_{\odot}$ (Piro et al. 2021), while the extended Type IIb SN 1993J exhibits a much larger envelope mass of $\sim 0.2 \,\mathrm{M}_{\odot}$ (Woosley et al. 1994). Similarly, the envelope radius of SN 2024iss is larger than that of the compact SN 2008ax (~ $40\,R_{\odot}$; Folatelli et al. 2015), but smaller than that of SN 1993J ($\sim 575~R_{\odot}$; Woosley et al. 1994). Additionally, as illustrated in Fig. 13, the X-ray luminosity of SN 2024iss is overall higher than that of Type IIb SNe with a less extended envelope, e.g., SNe 2011dh and 2016gkg, but lower than that of SN 1993J, whose progenitor had a more massive and extended hydrogen envelope. Taken together, the envelope properties and X-ray emission suggest that SN 2024iss likely represents a transitional object lying between the compact and extended subtypes of Type IIb SNe.

To further investigate the properties of SN 2024iss and the CSM-envelope connection, following Maeda et al. (2015), we plot in Figure 14 the mass-loss rate per unit wind velocity (\dot{M}/v_w) against the envelope radius. The choice of the former parameter minimizes the uncertainties due to the assumption of wind velocities. The mass-loss rates are estimated from the X-ray analyses of SNe 1993J (Fransson et al. 1996),

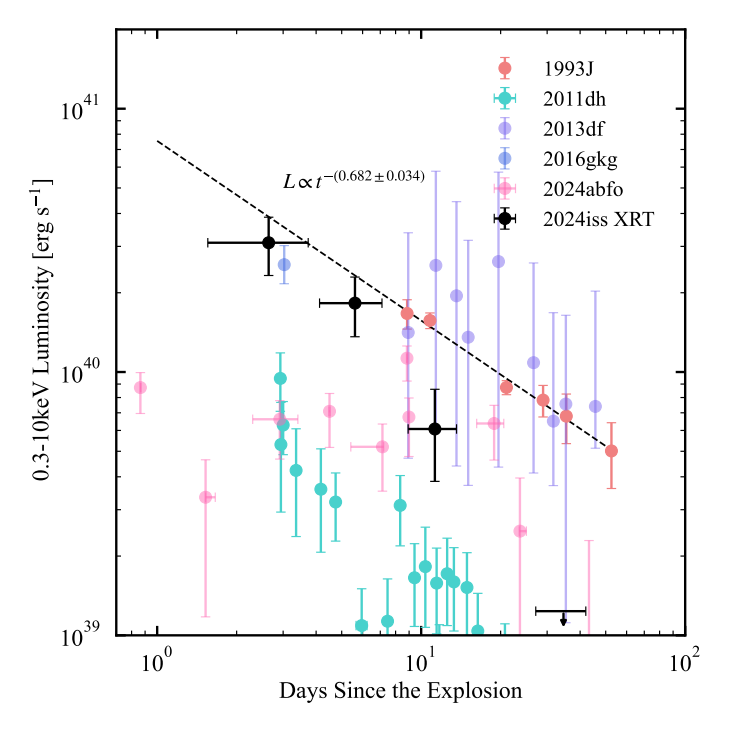


Fig. 13: The 0.3–10 keV X-ray luminosity evolution of SN 2024iss, compared with those of SNe 1993J (Chandra et al. 2009), 2011dh (Soderberg et al. 2012), 2013df (Kamble et al. 2016), 2016gkg (Dwarkadas 2025), and 2024abfo (Reguitti et al. 2025). While most of the comparison data are in the 0.3–10 keV band, the fluxes of SNe 1993J and 2013df were measured in the 0.3–8 keV band.

2008ax (Roming et al. 2009), 2011dh (Maeda et al. 2014), and 2013df (Kamble et al. 2016). The mass-loss rate of SN 2013df was adopted from Bufano et al. (2014a), based on an analysis of its radio light curves. The progenitor radius was inferred through a comparison between the SED yielded from archival pre-explosion images obtained by the *Hubble Space Telescope* and stellar evolution tracks, i.e., SNe 1993J (Maund et al. 2004), 2011dh (Maund et al. 2011), 2013df (Van Dyk et al. 2014), and 2008ax (Folatelli et al. 2015). The progenitor radius of SN 2011hs was inferred by modeling its bolometric light curve (Bufano et al. 2014b). We adopt the progenitor radii of Type Ib/c SNe from Maeda et al. (2012). The massloss rates of Type Ib/c SNe were inferred from their radio light curves, assuming a typical wind velocity of ~1000 km s⁻¹ (Chevalier & Fransson 2006).

As shown in Fig. 14, SN 2024iss lies in between the eIIb and cIIb groups. This supports the empirical relation proposed by Maeda et al. (2015), where more extended progenitors tend to have experienced a stronger mass loss. Although SN 2024iss seems to have a smaller progenitor radius compared to that of SN 2011dh, this discrepancy may stem from systematic differences in envelope radii as estimated from the light curve fitting and comparison between the progenitor SED and stellar evolution models. Moreover, there exists a transitional subtype between SNe IIL and SNe IIb, Type II short-plateau SNe. These events show plateaus lasting only several tens of days, and are characterized by relatively massive hydrogen envelopes ($\sim 1.7 \, M_{\odot}$) and high mass-loss rates of $\sim 10^{-2} \, M_{\odot}$ yr⁻¹, as in-

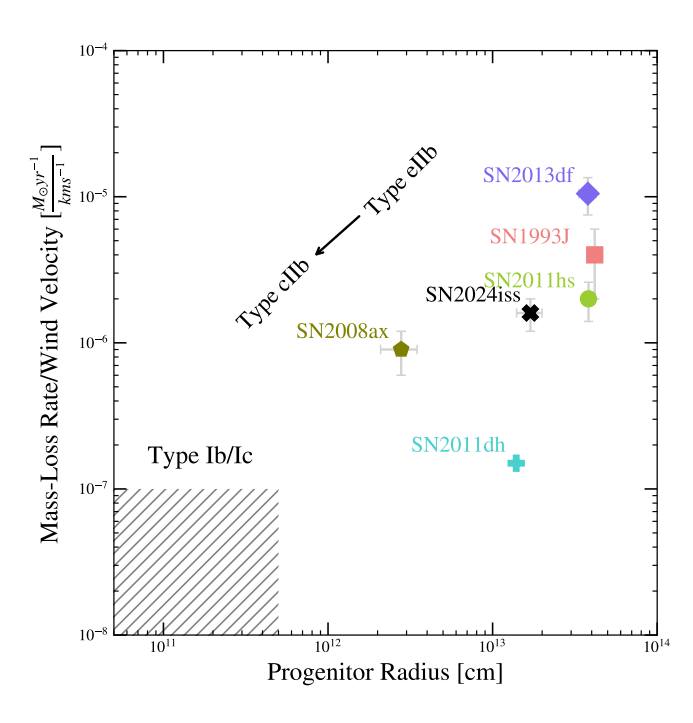


Fig. 14: Comparison between the mass-loss rate normalized by wind velocity (\dot{M}/ν_w) and the progenitor radius. The shaded region indicates typical CSM densities of Type Ib/c SNe(Chevalier & Fransson 2006), though these estimates may suffer from systematic uncertainties of up to an order of magnitude (Maeda et al. 2012). Color-coded symbols represent the estimated values for different SNe as labeled. The upper-right to lower-left arrow illustrates a possible evolutionary sequence from Type eIIb to cIIb and eventually to Type Ib/Ic SNe.

ferred for the sample presented by Hiramatsu et al. (2021). Furthermore, Farah et al. (2025a) classified transitional IIb events lying between Type II short-plateau SNe and Type IIb SNe, with envelope masses of around $0.6-0.8\,M_{\odot}$. We expect Type II short-plateau SNe and these transitional Type IIb SNe to emerge in the upper-right region of Fig. 14, offering further insights into the relationship between CSM and envelope in hydrogen-rich SNe.

7.3. Implications of the Low Ejecta Mass of SN 2024iss

The Arnett model fit to the bolometric light curve of SN 2024iss suggests an ejecta mass of $1.27\pm0.34\,M_{\odot}$ and a ^{56}Ni mass of $0.117\pm0.013\,M_{\odot}$. While the latter is consistent with the average value derived for SNe IIb, the ejecta mass of SN 2024iss is lower than all SNe compiled in Taddia et al. (2018). The faint and fast Type IIb SN 2011hs exhibits a similar ejecta mass and explosion energy compared to that of SN 2024iss, but with a significantly lower ^{56}Ni mass (Bufano et al. 2014a).

The secondary peak of SN 2024iss reached $M_V = -17.43 \pm 0.26$, which is consistent with the average of -17.4 mag from the sample in (Taddia et al. 2018). However, it appears to be a faster decliner as indicated by its $\Delta m_{15}(V) = 1.13$ mag (see Section 3.4), compared to the mean value of 0.93 mag inferred for SNe IIb (Taddia et al. 2018). The late-time decay rate also approaches 2 mag per 100 days, one of the steepest in the sample. This is consistent with the trend reported by Taddia et al. (2018),

where objects with larger $\Delta m_{15}(V)$ also exhibit a steeper late-time decline. Taddia et al. (2018) explained this trend by noting that objects with higher $E_{\rm K}/M_{\rm ej}$ ratios are less efficient in trapping gamma-rays, and therefore exhibit a steeper late-time decline and a narrower light-curve peak.

Prentice et al. (2018) found that the ejecta masses of SNe IIb exhibited a bimodal distribution peaking at 1.9 and 3.9 M_{\odot} , as represented by SNe 1993J ($M_{\rm ej}\approx 2.2\,\rm M_{\odot}$, Lyman et al. 2016) and 2016gkg ($M_{\rm ej}\approx 3.4\,\rm M_{\odot}$, Bersten et al. 2018), respectively. Such a bimodal mass distribution of the ejecta may indicate a discontinuity of the intrinsic properties of Type IIb SNe with one group having more extended and the other having a rather compact envelope. The ejecta mass of SN 2024iss falls within the lower ejecta mass regime, consistent with its Type eIIb classification.

Ayala et al. (2025) also found that although the inferred 56 Ni masses of Type eIIb and cIIb SNe are similar, the former group tends to have a lower average ejecta mass. Das et al. (2023) studied a sample of Ca-rich SNe IIb, which exhibit low ejecta masses and are inferred to originate from progenitors with $M_{\rm ZAMS} < 12~M_{\odot}$. They suggest that progenitors with smaller initial masses may develop larger envelope radii. According to Dewi et al. (2002); Dewi & Pols (2003), a progenitor star with such an extended envelope may expand sufficiently to fill their Roche lobes again and undergo additional episodes of mass transfer. This process can further strip the envelope and enrich the CSM, thus compatible with low ejecta mass observed in SN 2024iss.

Taken together, these results indicate that Type eIIb and cIIb SNe may arise from progenitors with similar initial ZAMS masses but diverge in their final envelope and ejecta properties. The interaction with its companion star may provide one natural explanation. In particular, an enhanced CSM enrichment during the common-envelope phase may take place before the SN explosion. Maeda et al. (2022) emphasized that instead of the initial mass of the exploding star, the binary separation and the orbital period may play a more critical role in determining the observational properties of SN explosion.

It is important to note, however, that the Arnett model assumes a constant opacity and fixed photospheric velocity, which may introduce systematic uncertainties in the derived parameters. For instance, adopting a photospheric velocity of 15,000 km s⁻¹ following Yamanaka et al. (2025), the Arnett model yields a larger ejecta mass of $M_{\rm ej} = 2.64 \pm 0.53~M_{\odot}$, but the corresponding kinetic energy ($E_k = 3.54 \pm 0.83 \times 10^{51} \text{erg}$) would be unrealistically high for a Type IIb SN. Alternatively, if we adopt an opacity of $\kappa = 0.2 \,\mathrm{cm}^2 \,\mathrm{g}^{-1}$ as suggested by Nagy & Vinkó (2016) and maintain the same photospheric velocity of 15,000 km s⁻¹, the fit yields $M_{\rm ej} = 1.23 \pm 0.23 \ M_{\odot}$ and $E_k = 1.64 \pm 0.3 \times 10^{51}$ erg. Taken together, these estimates imply an ejecta mass in the range of 1.23–2.64 M_{\odot} . However, considering the steep decline of the radioactive tail, a lower ejecta mass appears more plausible for SN 2024iss. With additional data obtained during the nebular phase, it should be possible to better constrain the ejecta mass following Wheeler et al. (2015) and Haynie & Piro (2023).

7.4. The mass-loss history of SN 2024iss: a confined structure

As discussed in Section 6, the column density of neutral hydrogen estimated from the X-ray spectrum of SN 2024iss suggests that by the time of the first detection, the CSM was already engulfed by the SN ejecta. The extension of the former is therefore confined within a radius of $\sim 1.3 \times 10^{14}$ cm. Assuming a wind velocity of $10 \, \mathrm{km \, s^{-1}}$, this constrains the mass ejection to take place no earlier than four years before the explosion. For a progenitor star with a ZAMS mass of 9-11 M_{\odot} , the episode of such a mass-loss wind coincides with the carbon shell burning phase or the onset of neon burning (Woosley et al. 2002). If the eruptive mass loss originates from instabilities intrinsic to the star, it may be triggered by mechanisms such as pulsation-driven superwinds (Yoon & Cantiello 2010), turbulent convection fluctuations (David Arnett & Meakin 2011), wavedriven mass loss during late burning stages (Shiode & Quataert 2013; Wu & Fuller 2020), or core neutrino emission (Moriya 2014). Alternatively, if the eruption results from a binary interaction, it supports the late Case B mass transfer scenario for Type eIIb progenitors proposed by Yoon et al. (2017), in which mass loss continues up to the time of the SN explosion.

The confined CSM structure inferred from the early X-ray observations of SN 2024iss may be a ubiquitous configuration for certain subtypes of Type IIb SNe. As suggested by Gal-Yam et al. (2014), an enhanced mass loss during the final year prior to the explosion can inflate the apparent photospheric radius of the progenitor, potentially causing a Type cIIb to appear as having an extended envelope. This effect may explain the discrepancy between the progenitor radii inferred from the stellar evolution model fitting to the SED of the progenitor star detected in archival images and the shock-cooling model fitting to the early bolometric light curves of the SN.

Although current observations indicate that SN 2024iss has a confined CSM, the presence of CSM further away remains uncertain. The boxy hydrogen structure observed in the nebular spectra of SN 1993J suggests a hydrogen-rich CSM at large radii (Matheson et al. 2000). Given the similarities between SN 1993J and SN 2024iss, the nebular spectra of SN 2024iss may enable a more comprehensive probe of the mass loss history of SN 2024iss.

The synergy of estimating the mass loss rate and the envelope properties of Type IIb SNe may enable stringent constraints on the framework of binary interactions (Ouchi & Maeda 2017). The progenitor system of SN 2024iss must satisfy two conditions: the envelope shall retain sufficient mass, and the mass-loss rate should be sufficiently high over the final years to build up a rather confined and dense CSM content.

8. Conclusion

We present optical, UV and X-ray observations of SN 2024iss, a Type IIb SN with a prominent double peak in optical bands and bright thermal X-ray emission. We summarize our key findings as follows:

⁹ The relevant data and analysis will be presented in a forthcoming paper.

- 1. The optical light curves of SN 2024iss exhibit a double-peak feature. The first V-band peak, which can be attributed to shock cooling, occurred at ~2.4 days after the explosion and reached a peak magnitude of $M_V = -17.33 \pm 0.26$. The second peak, powered by ⁵⁶Ni decay, reached a peak magnitude of $M_V = -17.43 \pm 0.26$ at ~ 18.7 days after the SN explosion. The photometric follow-up campaign on SN 2024iss was carried out starting from ~0.87 days after the last non-detection, which corresponds to about 0.44 days after the SN explosion. The prompt observations make SN 2024iss one of the most well-sampled SNe IIb during the early phases.
- 2. We measure a photospheric velocity of SN 2024iss to be $\sim 19,400\,\mathrm{km\,s^{-1}}$ from the absorption minimum of the P Cygni profile of H α in the earliest spectrum obtained at day 3.82. The velocity decreased to $\sim 13,600\,\mathrm{km\,s^{-1}}$ after the secondary peak of the V-band light curve. The H α and H β features remain detectable in our last spectrum obtained at $t\approx 87$ days after the SN explosion, indicating the presence of a hydrogen-rich ejecta, which is similar to that observed in SN 1993J (Filippenko et al. 1994).
- 3. We fit the second peak of the pseudo-bolometric light curve of SN 2024iss with an Arnett-like model and adopt a photospheric velocity of 7500 km s⁻¹ based on the Fe II λ 5169 line measured around the V-band maximum. The best-fitting parameters are $M_{\rm Ni}=0.117\pm0.013~M_{\odot},~M_{\rm ej}=1.272\pm0.343~M_{\odot}$ and $E_k=0.427\pm0.115\times10^{51}{\rm erg}$. The inferred ⁵⁶Ni mass is typical for Type IIb SNe, while the relatively low ejecta mass is compatible with the rapid decline in luminosity, as indicated by the large Δm_{15} value of 1.13 mag, compared to an average of 0.93 mag for Type IIb SNe (Taddia et al. 2018).
- 4. We fit the multiband shock-cooling peak of SN 2024iss using the P21 model, which provides a plausible description of the data. The best-fit parameters are: $R_{\rm env} = 244 \pm 43 \ R_{\odot}$, $M_{\rm env} = 0.11 \pm 0.04 \ M_{\odot}$, and $v_{\rm s} = (1.67 \pm 0.07) \times 10^4 \ {\rm km \ s^{-1}}$.
- 5. SN 2024iss exhibits bright thermal bremsstrahlung emission from the forward shock. The strength of the emission is comparable to that observed in SNe 1993J and 2013df. Assuming a wind velocity of $10\,\mathrm{km\,s^{-1}}$, the best fit to the X-ray light curve of SN 2024iss indicates a mass loss rate of $\dot{M}=1.6\times10^{-5}\,M_\odot\,\mathrm{yr^{-1}}$ and a shock velocity of $9.5\times10^8\,\mathrm{cm\,s^{-1}}$. An independent estimate based on the EM gives a slightly higher massloss rate of $(5.55\pm1.57)\times10^{-5}\,M_\odot\,\mathrm{yr^{-1}}$.
- 6. The low column density of neutral hydrogen of SN 2024iss placed a stringent constraints on the extension of the CSM within a radius of $R \lesssim 1.3 \times 10^{14}$ cm. Assuming a wind velocity of 10 km s^{-1} , this indicates that a significant mass ejection may have occurred within about four years prior to the SN explosion.

The combination of the optical and X-ray observations provides a powerful approach to probe the physical properties of SESNe. In particular, the prompt X-ray emissions from SNe obtained within the first hours after the explosion, as facilitated by wide-field sky surveys such as EP (Yuan et al. 2022), will enable a systematic characterization of their immediate environment and shed light on the mass-loss process and explosion mechanisms of SESNe.

9. Acknowledgements

We thank Yi Yang for helpful suggestions on the writing and for valuable discussions. This work is supported by the National Science Foundation of China (NSFC grants 12288102 and 12033003), the Tencent Xplorer Prize, and the Ma Huateng Foundation. The LCO group is supported by U.S. National Science Foundation (NSF) grants AST-1911151 and AST-2308113. Jujia Zhang is supported by the National Key Research and Development Program of China (NKRDPC) with grant 2021YFA1600404, the NSFC(grants 12173082, 12333008, and 12225304), the Yunnan Fundamental Research Projects (YFRP; grants 202501AV070012, 202401BC070007, 202201AT070069, and 202501AS070005), the Top-notch Young Talents Program of Yunnan Province, the Light of West China Program provided by the Chinese Academy of Sciences (CAS), and the International Centre of Supernovae, Yunnan Key Laboratory (grant 202302AN360001). WXL is supported by NSFC (12120101003 and 12373010), the National Key R&D Program (2022YFA1602902 and 2023YFA1607804), and Strategic Priority Research Program of CAS (XDB0550100 and XDB0550000).

Time-domain research by the University of Arizona team and D.J.S. is supported by NSF grants AST-2108032, AST-2308181, AST-2407566, and AST-2432036, and the Heising-Simons Foundation under grant 2020-1864. A.P., A.R., and G.V. acknowledge support from the PRIN-INAF 2022 project "Shedding light on the nature of gap transients: from the observations to the model." A.R. also acknowledges financial support from the GRAWITA Large Program Grant (PI P. D'Avanzo). Y.-Z. Cai is supported by NSFC (grant 12303054), the NKRDPC (grant 2024YFA1611603), the YFRP (grants 202401AU070063, 202501AS070078), and the International Centre of Supernovae, Yunnan Key Laboratory (grant 202302AN360001). J.V. is supported by the NKFIH-OTKA Grant K142534. Maokai Hu is funded by China Postdoctoral Science Foundation (Certificate Number 2025T180872). This work is sponsored by the Natural Science Foundation of Xinjiang Uygur Autonomous Region under grant 2024D01D32, Tianshan Talent Training Program grants 2023TSYCLJ0053 and 2023TSYCCX0101, the Central Guidance for Local Science and Technology Development Fund under grant ZYYD2025QY27, and the NSFC (grants 12433007, 12373038). A.V.F.'s research group at UC Berkeley acknowledges financial assistance from the Christopher R. Redlich Fund, as well as donations from Gary and Cynthia Bengier, Clark and Sharon Winslow, Alan Eustace and Kathy Kwan, William Draper, Timothy and Melissa Draper, Briggs and Kathleen Wood, Sanford Robertson (W.Z. is a Bengier-Winslow-Eustace Specialist in Astronomy, T.G.B. is a Draper-Wood-Robertson Specialist in Astronomy), and numerous other donors.

This study uses observations obtained with the Hobby-Eberly Telescope, which is a joint project of the University of Texas at Austin, the Pennsylvania State University, Ludwig-Maximilians-Universität München, and Georg-August-Universität Göttingen. The HET is named in honor of its principal benefactors, William P. Hobby and Robert E. Eberly. The Low Resolution Spectrograph 2 (LRS2) was developed and

funded by the University of Texas at Austin McDonald Observatory and Department of Astronomy and by Pennsylvania State University. We thank the Leibniz-Institut für Astrophysik Potsdam (AIP) and the Institut für Astrophysik Göttingen (IAG) for their contributions to the construction of the integral field units.

Based in part on observations obtained as part of (GN-2024A-Q-403; P.I. Jennifer Andrews) at the international Gemini Observatory, a program of the U.S. NSF NOIRLab, which is managed by the Association of Universities for Research in Astronomy (AURA) under a cooperative agreement with the U.S. NSF on behalf of the Gemini Observatory partnership: the NSF (United States), National Research Council (Canada), Agencia Nacional de Investigación y Desarrollo (Chile), Ministerio de Ciencia, Tecnología e Innovación (Argentina), Ministério da Ciência, Tecnologia, Inovações e Comunicações (Brazil), and Korea Astronomy and Space Science Institute (Republic of Korea). These observations were processed using DRAGONS (Data Reduction for Astronomy from Gemini Observatory North and South). This work was enabled by observations made from the Gemini North telescope, located within the Maunakea Science Reserve and adjacent to the summit of Maunakea. We are grateful for the privilege of observing the Universe from a place that is unique in both its astronomical quality and its cultural significance.

The LBT is an international collaboration among institutions in the United States, Italy, and Germany. LBT Corporation Members are The University of Arizona on behalf of the Arizona Board of Regents; Istituto Nazionale di Astrofisica, Italy; LBT Beteiligungsgesellschaft, Germany, representing the Max-Planck Society, The Leibniz Institute for Astrophysics Potsdam, and Heidelberg University; The Ohio State University, and The Research Corporation, on behalf of The University of Notre Dame, University of Minnesota, and University of Virginia. A major upgrade of the Kast spectrograph on the Shane 3 m telescope at Lick Observatory, led by Brad Holden, was made possible through generous gifts from the Heising-Simons Foundation, William and Marina Kast, and the University of California Observatories. Research at Lick Observatory is partially supported by a generous gift from Google.

This paper made use of the modsCCDRed data-reduction code developed in part with funds provided by NSF grants AST-9987045 and AST-1108693. Some observations reported here were obtained at the MMT Observatory, a joint facility of the University of Arizona and the Smithsonian Institution. We acknowledge the observational data taken at Einstein Probe (EP), a space mission supported by the Strategic Priority Program on Space Science of the Chinese Academy of Sciences, in collaboration with ESA, MPE, and CNES (grant XDA15310000), the Strategic Priority Research Program of the Chinese Academy of Sciences (grant XDB0550200) and the NKRDPC (grant 2022YFF0711500). We also acknowledge the observational data taken with Swift and NuSTAR.

References

Arcavi, I., Gal-Yam, A., Yaron, O., et al. 2011, ApJ, 742, L18
Arcavi, I., Hosseinzadeh, G., Brown, P. J., et al. 2017, The Astrophysical Journal Letters, 837, L2

Arnett, W. D. 1982, ApJ, 253, 785

Ayala, B., Anderson, J. P., Pignata, G., et al. 2025, arXiv e-prints, arXiv:2503.05909

Bai, C.-H., Feng, G.-J., Zhang, X., et al. 2020, Research in Astronomy and Astrophysics, 20, 211

Barbieri, C., Bhatia, R. K., Bonoli, C., et al. 1994, in Advanced Technology Optical Telescopes V, ed. L. M. Stepp, Vol. 2199, International Society for Optics and Photonics (SPIE), 10 – 21

Barbon, R., Benetti, S., Cappellaro, E., et al. 1995, A&AS, 110, 513

Bellm, E. C., Kulkarni, S. R., Graham, M. J., et al. 2019, PASP, 131, 018002

Benetti, S., Patat, F., Turatto, M., et al. 1994, A&A, 285, L13

Bersten, M. C., Folatelli, G., García, F., et al. 2018, Nature, 554, 497

Breeveld, A. A., Landsman, W., Holland, S. T., et al. 2011, in American Institute of Physics Conference Series, Vol. 1358, Gamma Ray Bursts 2010, ed. J. E. McEnery, J. L. Racusin, & N. Gehrels, 373–376

Brennan, S. J. & Fraser, M. 2022, A&A, 667, A62

Brown, T. M., Baliber, N., Bianco, F. B., et al. 2013, PASP, 125, 1031

Bufano, F., Pignata, G., Bersten, M., et al. 2014a, MNRAS, 439, 1807

Bufano, F., Pignata, G., Bersten, M., et al. 2014b, MNRAS, 439, 1807

Burrows, D. N., Hill, J. E., Nousek, J. A., et al. 2005, Space Sci. Rev., 120, 165 Cardelli, J. A., Clayton, G. C., & Mathis, J. S. 1989, ApJ, 345, 245

Chandra, P., Dwarkadas, V. V., Ray, A., Immler, S., & Pooley, D. 2009, ApJ, 699, 388

Chen, Y., Cui, W., Han, D., et al. 2020, in Society of Photo-Optical Instrumentation Engineers (SPIE) Conference Series, Vol. 11444, Space Telescopes and Instrumentation 2020: Ultraviolet to Gamma Ray, ed. J.-W. A. den Herder, S. Nikzad, & K. Nakazawa, 114445B

Chevalier, R. A. & Fransson, C. 2006, ApJ, 651, 381

Chevalier, R. A. & Fransson, C. 2017, Thermal and Non-thermal Emission from Circumstellar Interaction (Springer International Publishing), 875–937

Chevalier, R. A. & Soderberg, A. M. 2010, The Astrophysical Journal, 711, L40
Chonis, T. S., Hill, G. J., Lee, H., Tuttle, S. E., & Vattiat, B. L. 2014, in Ground-Based and Airborne Instrumentation for Astronomy V, Vol. 9147 (International Society for Optics and Photonics), 91470A

Das, K. K., Kasliwal, M. M., Fremling, C., et al. 2023, The Astrophysical Journal, 959, 12

David Arnett, W. & Meakin, C. 2011, The Astrophysical Journal, 741, 33Dessart, L., Gutiérrez, C. P., Ercolino, A., Jin, H., & Langer, N. 2024, A&A, 685, A169

Dessart, L. & Hillier, D. J. 2005, A&A, 439, 671

Dewi, J. D. M. & Pols, O. R. 2003, MNRAS, 344, 629

Dewi, J. D. M., Pols, O. R., Savonije, G. J., & van den Heuvel, E. P. J. 2002, MNRAS, 331, 1027

Dong, Y., Valenti, S., Ashall, C., et al. 2024, The Astrophysical Journal, 974, 316Dwarkadas, V. V. 2025, On the X-ray Emission From Supernovae, and Implications for the Mass-Loss Rates of their Progenitor Stars

Ergon, M., Sollerman, J., Fraser, M., et al. 2014, Astronomy & Astrophysics, 562, A17

Evans, P. A., Beardmore, A. P., Page, K. L., et al. 2009, Monthly Notices of the Royal Astronomical Society, 397, 1177

Evans, P. A., Beardmore, A. P., Page, K. L., et al. 2007, A&A, 469, 379

Fabricant, D., Fata, R., Epps, H., et al. 2019, PASP, 131, 075004

Fan, Y.-F., Bai, J.-M., Zhang, J.-J., et al. 2015, Research in Astronomy and Astrophysics, 15, 918

Farah, J. R., Howell, D. A., Hiramatsu, D., et al. 2025a, When IIb Ceases To Be: Bridging the Gap Between IIb and Short-plateau Supernovae

Farah, J. R., Howell, D. A., Terreran, G., et al. 2025b, The Astrophysical Journal, 984, 60

 $Filippenko,\,A.\,\,V.\,\,1997,\,Annual\,\,Review\,\,of\,\,Astronomy\,\,and\,\,Astrophysics,\,35,\,309$

Filippenko, A. V., Matheson, T., & Barth, A. J. 1994, AJ, 108, 2220

Filippenko, A. V., Matheson, T., & Ho, L. C. 1993, ApJ, 415, L103

Fixsen, D. J., Cheng, E. S., Gales, J. M., et al. 1996, ApJ, 473, 576

Foight, D. R., Güver, T., Özel, F., & Slane, P. O. 2016, ApJ, 826, 66

Folatelli, G., Bersten, M. C., Kuncarayakti, H., et al. 2015, ApJ, 811, 147

Foreman-Mackey, D., Hogg, D. W., Lang, D., & Goodman, J. 2013, Publications of the Astronomical Society of the Pacific, 125, 306

Fransson, C. & Chevalier, R. A. 1989, ApJ, 343, 323

Fransson, C., Lundqvist, P., & Chevalier, R. A. 1996, ApJ, 461, 993

Fukugita, M., Ichikawa, T., Gunn, J. E., et al. 1996, AJ, 111, 1748

Gal-Yam, A. 2017, Observational and Physical Classification of Supernovae (Springer International Publishing), 195–237

Gal-Yam, A., Arcavi, I., Ofek, E. O., et al. 2014, Nature, 509, 471

Gehrels, N., Chincarini, G., Giommi, P., et al. 2004, ApJ, 611, 1005

- Georgy, C. 2012, A&A, 538, L8
- Graham, M. J., Kulkarni, S. R., Bellm, E. C., et al. 2019, PASP, 131, 078001 Hachinger, S., Mazzali, P. A., Taubenberger, S., et al. 2012, MNRAS, 422, 70 Hamuy, M., Deng, J., Mazzali, P. A., et al. 2009, The Astrophysical Journal, 703, 1612
- Harrison, F. A., Craig, W. W., Christensen, F. E., et al. 2013, ApJ, 770, 103 Haynie, A. & Piro, A. L. 2023, The Astrophysical Journal, 956, 98
- Henden, A. A., Templeton, M., Terrell, D., et al. 2016, VizieR Online Data Catalog: AAVSO Photometric All Sky Survey (APASS) DR9 (Henden+, 2016), VizieR On-line Data Catalog: II/336. Originally published in: 2015AAS...22533616H
- Hiramatsu, D., Howell, D. A., Moriya, T. J., et al. 2021, The Astrophysical Journal, 913. 55
- Hook, I. M., Jørgensen, I., Allington-Smith, J. R., et al. 2004, PASP, 116, 425 Hosseinzadeh, G. & Gomez, S. 2020, Light Curve Fitting
- Huang, F., Li, J.-Z., Wang, X.-F., et al. 2012, Research in Astronomy and Astrophysics, 12, 1585
- Johnson, H. L., Mitchell, R. I., Iriarte, B., & Wisniewski, W. Z. 1966, Communications of the Lunar and Planetary Laboratory, 4, 99
- Jordi, K., Grebel, E. K., & Ammon, K. 2006, A&A, 460, 339
- Kamble, A., Margutti, R., Soderberg, A. M., et al. 2016, ApJ, 818, 111
- Kilpatrick, C. D., Coulter, D. A., Foley, R. J., et al. 2022, The Astrophysical Journal, 936, 111
- Kilpatrick, C. D., Foley, R. J., Abramson, L. E., et al. 2017, MNRAS, 465, 4650 Kochanek, C. S., Shappee, B. J., Stanek, K. Z., et al. 2017, PASP, 129, 104502 Kumar, B., Pandey, S. B., Sahu, D. K., et al. 2013, MNRAS, 431, 308
- Labrie, K., Anderson, K., Cárdenes, R., Simpson, C., & Turner, J. E. H. 2019, in Astronomical Society of the Pacific Conference Series, Vol. 523, Astronomical Data Analysis Software and Systems XXVII, ed. P. J. Teuben, M. W. Pound, B. A. Thomas, & E. M. Warner, 321
- Law, N. M., Kulkarni, S. R., Dekany, R. G., et al. 2009, PASP, 121, 1395 Li, G., Hu, M., Li, W., et al. 2024, Nature, 627, 754
- Liu, L.-D., Zhang, Y.-H., Yu, Y.-W., et al. 2025, TransFit: An Efficient Framework for Transient Light-Curve Fitting with Time-Dependent Radiative Diffusion
- Lyman, J. D., Bersier, D., James, P. A., et al. 2016, MNRAS, 457, 328
- Maeda, K., Chandra, P., Moriya, T. J., et al. 2022, The Astrophysical Journal, 942, 17
- Maeda, K., Hattori, T., Milisavljevic, D., et al. 2015, ApJ, 807, 35
- Maeda, K., Katsuda, S., Bamba, A., Terada, Y., & Fukazawa, Y. 2014, The Astrophysical Journal, 785, 95
- Maeda, K., Moriya, T., Kawabata, K., et al. 2012, Mem. Soc. Astron. Italiana, 83, 264
- Matheson, T., Filippenko, A. V., Ho, L. C., Barth, A. J., & Leonard, D. C. 2000, AJ, 120, 1499
- Maund, J. R., Fraser, M., Ergon, M., et al. 2011, ApJ, 739, L37
- Maund, J. R. & Smartt, S. J. 2009, Science, 324, 486
- Maund, J. R., Smartt, S. J., Kudritzki, R. P., Podsiadlowski, P., & Gilmore, G. F. 2004, Nature, 427, 129
- Medler, K., Mazzali, P. A., Teffs, J., et al. 2022, MNRAS, 513, 5540
- Medler, K., Mazzali, P. A., Teffs, J., et al. 2021, Monthly Notices of the Royal Astronomical Society, 506, 1832
- Miller, J. & Stone, R. 1994, The Kast Double Spectrograph
- Morag, J., Sapir, N., & Waxman, E. 2023, MNRAS, 522, 2764
- Morales-Garoffolo, A., Elias-Rosa, N., Benetti, S., et al. 2014, MNRAS, 445, 1647
- Morales-Garoffolo, A., Elias-Rosa, N., Bersten, M., et al. 2015, Monthly Notices of the Royal Astronomical Society, 454, 95
- Moriya, T. J. 2014, A&A, 564, A83
- Nagy, A. P. & Vinkó, J. 2016, Astronomy & Samp; Astrophysics, 589, A53
- Nakar, E. & Piro, A. L. 2014, ApJ, 788, 193
- Niu, Z., Sun, N.-C., & Liu, J. 2024, The Astrophysical Journal Letters, 970, L9Niu, Z., Sun, N.-C., Maund, J. R., et al. 2025, Discovery of a variable yellow supergiant progenitor for the Type IIb SN 2024abfo
- Oke, J. B. & Gunn, J. E. 1983, ApJ, 266, 713
- Orellana, M. & Bersten, M. C. 2022, A&A, 667, A92
- Ouchi, R. & Maeda, K. 2017, The Astrophysical Journal, 840, 90
- Piro, A. L. 2015, ApJ, 808, L51
- Piro, A. L., Haynie, A., & Yao, Y. 2021, The Astrophysical Journal, 909, 209Podsiadlowski, P. 1992, Publications of the Astronomical Society of the Pacific, 104, 717
- Pogge, R. 2019, rwpogge/modsCCDRed 2.0

- Pogge, R. W., Atwood, B., Brewer, D. F., et al. 2010, in Society of Photo-Optical Instrumentation Engineers (SPIE) Conference Series, Vol. 7735, Groundbased and Airborne Instrumentation for Astronomy III, ed. I. S. McLean, S. K. Ramsay, & H. Takami, 77350A
- Prentice, S. J., Ashall, C., James, P. A., et al. 2018, Monthly Notices of the Royal Astronomical Society, 485, 1559
- Prentice, S. J., Mazzali, P. A., Pian, E., et al. 2016, Monthly Notices of the Royal Astronomical Society, 458, 2973
- Prochaska, J., Hennawi, J., Westfall, K., et al. 2020, The Journal of Open Source Software, 5, 2308
- Rabinak, I. & Waxman, E. 2011, ApJ, 728, 63
- Ramsey, L. W., Adams, M. T., Barnes, T. G., et al. 1998, in Society of Photo-Optical Instrumentation Engineers (SPIE) Conference Series, Vol. 3352, Advanced Technology Optical/IR Telescopes VI, ed. L. M. Stepp, 34–42
- Rau, A., Kulkarni, S. R., Law, N. M., et al. 2009, PASP, 121, 1334
- Reguitti, A., Pastorello, A., Smartt, S. J., et al. 2025, SN 2024abfo: a partially stripped SN II from a yellow supergiant
- Richmond, M. W., Treffers, R. R., Filippenko, A. V., & Paik, Y. 1996, AJ, 112, 732
- Richmond, M. W., Treffers, R. R., Filippenko, A. V., et al. 1994, AJ, 107, 1022 Roming, P. W. A., Kennedy, T. E., Mason, K. O., et al. 2005, Space Sci. Rev., 120, 95
- Roming, P. W. A., Pritchard, T. A., Brown, P. J., et al. 2009, The Astrophysical Journal, 704, L118
- Ryder, S. D., Dyk, S. D. V., Fox, O. D., et al. 2018, The Astrophysical Journal, 856, 83
- Sana, H., de Mink, S. E., de Koter, A., et al. 2012, Science, 337, 444
- Sapir, N. & Waxman, E. 2017, ApJ, 838, 130
- Schlafly, E. F. & Finkbeiner, D. P. 2011, ApJ, 737, 103
- Shiode, J. H. & Quataert, E. 2013, The Astrophysical Journal, 780, 96
- Shivvers, I., Filippenko, A. V., Silverman, J. M., et al. 2019, MNRAS, 482, 1545
- Silverman, J. M., Mazzali, P., Chornock, R., et al. 2009, PASP, 121, 689 Smith, N. 2014, Annual Review of Astronomy and Astrophysics, 52, 487
- Smith, N. 2017, Interacting Supernovae: Types IIn and Ibn (Springer International Publishing), 403–429
- Soderberg, A. M., Margutti, R., Zauderer, B. A., et al. 2012, The Astrophysical Journal, 752, 78
- Soderberg, A. M., Margutti, R., Zauderer, B. A., et al. 2012, ApJ, 752, 78
- Spergel, D. N., Bean, R., Doré, O., et al. 2007, The Astrophysical Journal Supplement Series, 170, 377
- Sravan, N., Marchant, P., Kalogera, V., & Margutti, R. 2018, ApJ, 852, L17
- Sravan, N., Marchant, P., Kalogera, V., Milisavljevic, D., & Margutti, R. 2020, The Astrophysical Journal, 903, 70
- Steeghs, D., Galloway, D. K., Ackley, K., et al. 2022, Monthly Notices of the Royal Astronomical Society, 511, 2405
- Subrayan, B. M., Sand, D. J., Bostroem, K. A., et al. 2025, Early Shock-Cooling Observations and Progenitor Constraints of Type IIb SN 2024uwq
- Sukhbold, T., Ertl, T., Woosley, S. E., Brown, J. M., & Janka, H.-T. 2016, The Astrophysical Journal, 821, 38
- Szalai, T., Vinkó, J., Nagy, A. P., et al. 2016, MNRAS, 460, 1500
- Taddia, F., Stritzinger, M. D., Bersten, M., et al. 2018, A&A, 609, A136
- Tartaglia, L., Fraser, M., Sand, D. J., et al. 2017, ApJ, 836, L12
- Thorsett, S. E. & Chakrabarty, D. 1999, ApJ, 512, 288
- Tody, D. 1986, in Society of Photo-Optical Instrumentation Engineers (SPIE) Conference Series, Vol. 627, Instrumentation in astronomy VI, ed. D. L. Crawford, 733
- Tody, D. 1993, in Astronomical Society of the Pacific Conference Series, Vol. 52, Astronomical Data Analysis Software and Systems II, ed. R. J. Hanisch, R. J. V. Brissenden, & J. Barnes, 173
- Tonry, J. L., Denneau, L., Heinze, A. N., et al. 2018, PASP, 130, 064505
- Tsvetkov, D. Y., Volkov, I. M., Sorokina, E. I., et al. 2012, Photometric observations and preliminary modeling of type IIb supernova 2011dh
- Valenti, S., Elias-Rosa, N., Taubenberger, S., et al. 2008, ApJ, 673, L155
- Valenti, S., Sand, D., Pastorello, A., et al. 2014, MNRAS, 438, L101
- Van Dyk, S. D., Zheng, W., Fox, O. D., et al. 2014, The Astronomical Journal, 147, 37
- Van Dyk, S. D., Zheng, W., Fox, O. D., et al. 2014, AJ, 147, 37
- Wang, C.-J., Bai, J.-M., Fan, Y.-F., et al. 2019, Research in Astronomy and Astrophysics. 19, 149
- Waxman, E. & Katz, B. 2017, in Handbook of Supernovae, ed. A. W. Alsabti & P. Murdin. 967

- Wheeler, J. C., Johnson, V., & Clocchiatti, A. 2015, Monthly Notices of the Royal Astronomical Society, 450, 1295
- Woosley, S. E., Eastman, R. G., Weaver, T. A., & Pinto, P. A. 1994, ApJ, 429, 300
- Woosley, S. E., Heger, A., & Weaver, T. A. 2002, Reviews of Modern Physics, 74, 1015
- Woosley, S. E., Langer, N., & Weaver, T. A. 1993, ApJ, 411, 823
- Woosley, S. E., Pinto, P. A., & Hartmann, D. 1989, ApJ, 346, 395
- Wu, S. & Fuller, J. 2020, The Astrophysical Journal, 906, 3
- Yamanaka, M., Nagayama, T., & Horikiri, T. 2025, PASJ[arXiv:2503.05054]
- Yaron, O. & Gal-Yam, A. 2012, PASP, 124, 668
- Yoon, S.-C. 2017, MNRAS, 470, 3970
- Yoon, S.-C. & Cantiello, M. 2010, The Astrophysical Journal Letters, 717, L62 Yoon, S.-C., Dessart, L., & Clocchiatti, A. 2017, The Astrophysical Journal, 840,
- Yuan, W., Zhang, C., Chen, Y., & Ling, Z. 2022, The Einstein Probe Mission (Springer Nature Singapore), 1–30
- ¹ Department of Physics, Tsinghua University, Beijing, 100084, China
- National Astronomical Observatories, Chinese Academy of Sciences, Beijing 100101, China
- ³ School of Astronomy and Space Science, University of Chinese Academy of Sciences, Beijing 100049,1408, People's Republic of China
- ⁴ Las Cumbres Observatory
- ⁵ University of California, Santa Barbara, Department of Physics
- ⁶ Università degli Studi di Padova, Dipartimento di Fisica e Astronomia, Vicolo dell'Osservatorio 2, 35122 Padova, Italy
- 7 INAF Osservatorio Astronomico di Padova, Vicolo dell'Osservatorio 5, 35122 Padova, Italy
- 8 INAF Osservatorio Astronomico di Brera, Via Bianchi 46, 23807 Merate (LC), Italy
- ⁹ Department of Astronomy, University of California, Berkeley, CA 94720-3411, USA
- Yunnan Observatories, Chinese Academy of Sciences, Kunming 650216, China 10
- ¹¹ International Centre of Supernovae, Yunnan Key Laboratory, Kunming 650216, China 11
- Key Laboratory for the Structure and Evolution of Celestial Objects, Chinese Academy of Sciences, Kunming 650216, China 12
- ¹³ Steward Observatory, University of Arizona, 933 North Cherry Avenue, Tucson, AZ 85721-0065, USA
- ¹⁴ Gemini Observatory, 670 North A'ohoku Place, Hilo, HI 96720-2700, USA
- 15 LSSTC Catalyst Fellow
- ¹⁶ Xinjiang Astronomical Observatory, Chinese Academy of Sciences, Urumqi, Xinjiang, 830011, China
- ¹⁷ Università degli Studi di Padova, Dipartimento di Fisica e Astronomia, Vicolo dell'Osservatorio 3, 35122 Padova, Italy
- ¹⁸ Department of Astronomy, University of Texas, Austin, TX, 78712, USA
- 19 Kavli Institute for Theoretical Physics
- 20 Johns Hopkins University
- 21 School of Physics and Astronomy, Monash University, Clayton, Australia
- OzGrav: The ARC Center of Excellence for Gravitational Wave Discovery, Australia
- ²³ Adler Planetarium
- ²⁴ HUN-REN CSFK Konkoly Observatory, MTA Center of Excellence, Konkoly Thege ut 15-17, Budapest, 1121, Hungary
- Department of Experimental Physics, University of Szeged, Dóm tér 9, Szeged, 6720, Hungary
- ²⁶ ELTE Eötvös Loránd University, Institute of Physics and Astronomy, Pázmány Péter sétány 1/A, Budapest, 1117 Hungary

- ²⁷ Institute of High Energy Physics, Chinese Academy of Sciences, Beijing, 100049, China
- ²⁸ Department of Scientific Research, Beijing Planetarium, Beijing 100044, China

Appendix A: X-ray and Optical Spectroscopic Observations

Table A.1: The X-ray Observations of SN 2024iss

Instrument	Start time	End time	Exposure	Phase ^a
	(UTC)	(UTC)	(second)	(day)
Swift-XRT	2024-05-13 18:18:31.00	2024-05-15 22:34:53.00	4939.62	1.95 ± 1.09
EP-FXT	2024-05-14 23:21:13.65	2024-05-15 08:08:30.80	17375.48	2.26 ± 0.18
Swift-XRT	2024-05-16 07:54:00.00	2024-05-19 07:29:53.00	5721.27	4.92 ± 1.49
NuSTAR	2024-05-17 16:11:09.00	2024-05-18 12:51:09.00	37069.35	5.20 ± 0.43
Swift-XRT	2024-05-21 03:10:22.00	2024-05-25 19:42:53.00	7394.45	10.58 ± 2.34
EP-FXT	2024-05-23 11:08:18.67	2024-05-23 15:10:13.84	8924.59	10.65 ± 0.08
NuSTAR	2024-06-02 00:21:09.00	2024-06-03 03:01:09.00	50139.94	20.67 ± 0.56
Swift-XRT	2024-06-08 08:58:29.00	2024-06-23 05:45:53.00	20605.16	33.91 ± 7.43
Swift-XRT	2024-11-13 17:42:04.00	2024-12-26 15:30:53.00	11982.10	206.29 ± 21.45
Swift-XRT	2025-02-06 19:42:21.00	2025-02-20 12:26:54.00	6458.06	276.77 ± 6.85

Notes. (a) Time respect to MJD=60,442.21.

Table A.2: Spectral property from X-ray Observation of SN 2024iss

Instrument	Phase ^a	N _{int}	kT	Norm	Flux ^b	Unabsorbed Flux ^b
	(day)	$(10^{22}cm^{-2})$	(keV)	$10^{-4} cm^{-5}$	$(erg/cm^2/s)$	$(erg/cm^2/s)$
Swift-XRT	1.95 ± 1.09	0.009	32.57	$7.75^{\pm 0.58}_{\pm 0.55}$	$1.44_{\pm 0.10}^{\pm 0.11} \times 10^{-12}$	$1.43^{\pm 0.11}_{\pm 0.10} \times 10^{-12}$
EP-FXT	2.26 ± 0.18	0.009	32.57	$7.19_{\pm 0.18}^{\pm 0.18}$	$1.29^{\pm0.03}_{\pm0.03} \times 10^{-12}$	$1.28^{\pm0.03}_{\pm0.03} \times 10^{-12}$
Swift-XRT	4.92 ± 1.49	0.009	32.57	$4.57^{\pm0.43}_{\pm0.40}$	$8.50^{\pm0.79}_{\pm0.75} \times 10^{-13}$	$8.43^{\pm0.78}_{\pm0.74} \times 10^{-13}$
NuSTAR	5.20 ± 0.43	0.009	$32.57_{\pm 4.65}^{\pm 6.93}$	$7.91_{\pm 0.23}^{\pm 0.23}$	$2.85^{\pm 0.27}_{\pm 0.21} \times 10^{-12}$	$2.85^{\pm0.27}_{\pm0.21} \times 10^{-12}$
Swift-XRT	10.58 ± 2.34	0.009	32.57	$1.52^{\pm 0.52}_{\pm 0.43}$	$2.83^{\pm0.96}_{\pm0.79} \times 10^{-13}$	$2.80^{\pm 0.95}_{\pm 0.78} \times 10^{-13}$
EP-FXT	10.65 ± 0.08	0.009	32.57	$0.97^{\pm 0.11}_{\pm 0.10}$	$1.73^{\pm 0.20}_{\pm 0.19} \times 10^{-13}$	$1.73^{\pm0.19}_{\pm0.18} \times 10^{-13}$
NuSTAR	20.67 ± 0.56	0.009	32.57	$0.69^{\pm0.09}_{\pm0.09}$	$2.49_{\pm 0.32}^{\pm 0.33} \times 10^{-13}$	$2.49_{\pm 0.32}^{\pm 0.33} \times 10^{-13}$
Swift-XRT	33.91 ± 7.43	0.009	32.57	< 0.24	$< 4.83 \times 10^{-14}$	$< 4.79 \times 10^{-14}$
Swift-XRT	206.29 ± 21.45	0.009	32.57	< 10.95	$< 2.04 \times 10^{-12}$	$< 2.02 \times 10^{-12}$
Swift-XRT	276.77 ± 6.85	0.009	32.57	< 0.29	$< 5.35 \times 10^{-14}$	$< 5.31 \times 10^{-14}$

Notes. ^(a) Time respect to MJD=60,442.21. ^(b) The absorbed flux and unabsorbed flux are in 0.5-10 keV for FXT, 0.3-10 keV for XRT, and 3-79 keV for NuSTAR. We adopt a fixed plasma temperature to the temperature estimated from the 4th observation in the column for all other observations. Because of the limited photon counts and the restricted energy coverage of FXT (0.5-10 keV), the plasma temperature (kT) of SN 2024iss at each epoch cannot be reliably constrained independently (see Section 2.4).

Table A.3: Log of Optical Spectroscopy of SN 2024iss

UT	MJD	Phase ¹⁰	Telescope	Instrument	Exposure Time (s)	Range (Å)
2024-05-13 12:37	60443.53	1.32	XLT	BFOSC	2100	3769-8911
2024-05-14 03:17	60444.14	1.93	MMT	Binospec	1800	3823-9214
2024-05-14 11:53	60444.50	2.29	FTS	FLOYDS	900	3300-10180
2024-05-14 14:00	60444.58	2.37	XLT	BFOSC	2100	3770-8909
2024-05-14 16:52	60444.70	2.49	LJT	YFOSC	600	3616-8920
2024-05-15 08:17	60445.35	3.14	Lick	Kast	300	3636-10752
2024-05-15 13:09	60445.55	3.34	XLT	BFOSC	1800	3776-8917
2024-05-16 00:44	60446.03	3.82	TNG	LRS	300	3450-10510
2024-05-16 17:05	60446.71	4.50	LJT	YFOSC	600	3615-8920
2024-05-17 12:44	60447.53	5.32	XLT	BFOSC	1800	3770-8909
2024-05-17 21:08	60447.88	5.67	GT	B&C	1800	5775-6975
2024-05-17 22:54	60447.95	5.74	GT	B&C	1200	3315-7889
2024-05-18 18:48	60448.78	6.57	LJT	YFOSC	900	3612-8917
2024-05-20 12:57	60450.54	8.33	XLT	BFOSC	1800	3770-8909
2024-05-22 20:36	60452.86	10.65	GT	B&C	1800	3314-7889
2024-05-24 10:05	60454.42	12.21	FTN	FLOYDS	600	3300-10180
2024-05-24 18:07	60454.76	12.55	LJT	YFOSC	900	3613-8918
2024-05-25 22:26	60455.93	13.72	GT	B&C	1800	3314-7887
2024-05-26 08:06	60456.34	14.13	FTN	FLOYDS	600	3300-10180
2024-05-26 12:34	60456.52	14.31	XLT	BFOSC	2100	3776-8919
2024-05-26 21:49	60456.91	14.70	GT	B&C	1200	3316-7889
2024-05-29 06:30	60459.27	17.06	HET	LRS2	1400	3640-10500
2024-05-29 07:26	60459.31	17.10	MMT	Binospec	1350	3826-9215
2024-05-30 07:32	60460.31	18.11	LBT	MODS1B	2400	3200-8918
2024-05-30 13:58	60460.58	18.37	XLT	BFOSC	1800	3774-8911
2024-06-01 06:38	60462.28	20.07	FTN	FLOYDS	600	3300-10180
2024-06-01 16:15	60462.68	20.47	LJT	YFOSC	900	3615-8920
2024-06-01 23:00	60462.96	20.75	GT	B&C	900	3316-7890
2024-06-04 07:00	60465.29	23.08	MMT	Binospec	1500	3823-9215
2024-06-04 21:14	60465.89	23.68	GT	B&C	1200	3317-7891
2024-06-05 10:12	60466.43	24.22	FTN	FLOYDS	600	3300-10180
2024-06-06 09:00	60467.38	25.17	Lick	Kast	300	3636-10750
2024-06-11 05:15	60472.22	30.01	Bok	B&C Spec	2400	4000-8000
2024-06-11 07:13	60472.30	30.09	FTN	FLOYDS	600	3300-10180
2024-06-11 16:41	60472.70	30.49	LJT	YFOSC	1000	3612-8918
2024-06-13 08:41	60474.36	32.15	Lick	Kast	400	3626-10756
2024-06-14	60475.00	32.79	GNT	GMOS	240	3300-10180
2024-06-16 21:10	60477.88	35.67	GT	B&C	1800	3317-7889
2024-06-17 06:31	60478.27	36.06	FTN	FLOYDS	900	3300-10180
2024-06-22	60483.00	40.79	GNT	GMOS	240	3300-10180
2024-06-26 08:08	60487.34	45.13	FTN	FLOYDS	900	3300-10180
2024-06-26 21:02	60487.88	45.67	GT	B&C	1200	3316-7890

A&A proofs: manuscript no. arxiv

Table A.3: Continued

UT	MJD	Phase	Telescope	Inst.	Exp.Time (s)	Range (Å)
2024-06-28 13:42	60489.57	47.36	XLT	BFOSC	2100	3777-8907
2024-06-30 07:23	60491.31	49.10	FTN	FLOYDS	900	3300-10180
2024-07-04 06:42	60495.28	53.07	FTN	FLOYDS	900	3300-10180
2024-07-08 07:46	60499.32	57.11	FTN	FLOYDS	900	3300-10180
2024-07-12	60503.00	60.79	GNT	GMOS	240	3300-10180
2024-07-12 07:37	60503.32	61.11	FTN	FLOYDS	900	3300-10180
2024-07-14 21:37	60505.90	63.69	GT	B&C	1800	3318-7889
2024-07-16 06:54	60507.29	65.08	FTN	FLOYDS	900	3300-10180
2024-07-26 06:01	60517.25	75.04	FTN	FLOYDS	1800	3300-10180
2024-08-02 04:25	60524.18	81.97	Lick	Kast	1200	3624-10720
2024-08-03 06:21	60525.26	83.05	FTN	FLOYDS	1800	3300-10180
2024-08-07 06:02	60529.25	87.04	FTN	FLOYDS	1800	3300-10180

Notes. (a) Time respect to MJD=60,442.21.